

Durham Research Online

Deposited in DRO:

17 July 2014

Version of attached file:

Accepted Version

Peer-review status of attached file:

Peer-reviewed

Citation for published item:

Eke, V.R. and Bartram, S.A. and Lane, D.A. and Smith, D. and Teodoro, L.F.A. (2014) 'Lunar polar craters - icy, rough or just sloping?', *Icarus*, 241 . pp. 66-78.

Further information on publisher's website:

<http://dx.doi.org/10.1016/j.icarus.2014.06.021>

Publisher's copyright statement:

NOTICE: this is the author's version of a work that was accepted for publication in *Icarus*. Changes resulting from the publishing process, such as peer review, editing, corrections, structural formatting, and other quality control mechanisms may not be reflected in this document. Changes may have been made to this work since it was submitted for publication. A definitive version was subsequently published in *Icarus*, 241, 2014, 10.1016/j.icarus.2014.06.021.

Additional information:

Use policy

The full-text may be used and/or reproduced, and given to third parties in any format or medium, without prior permission or charge, for personal research or study, educational, or not-for-profit purposes provided that:

- a full bibliographic reference is made to the original source
- a [link](#) is made to the metadata record in DRO
- the full-text is not changed in any way

The full-text must not be sold in any format or medium without the formal permission of the copyright holders.

Please consult the [full DRO policy](#) for further details.

Accepted Manuscript

Lunar polar craters – icy, rough or just sloping?

Vincent R. Eke, Sarah A. Bartram, David A. Lane, David Smith, Luis F.A. Teodoro

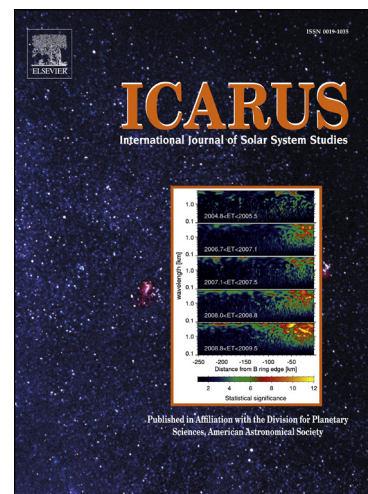
PII: S0019-1035(14)00332-7
DOI: <http://dx.doi.org/10.1016/j.icarus.2014.06.021>
Reference: YICAR 11152

To appear in: *Icarus*

Received Date: 6 January 2014
Revised Date: 16 June 2014
Accepted Date: 16 June 2014

Please cite this article as: Eke, V.R., Bartram, S.A., Lane, D.A., Smith, D., Teodoro, L.F.A., Lunar polar craters – icy, rough or just sloping?, *Icarus* (2014), doi: <http://dx.doi.org/10.1016/j.icarus.2014.06.021>

This is a PDF file of an unedited manuscript that has been accepted for publication. As a service to our customers we are providing this early version of the manuscript. The manuscript will undergo copyediting, typesetting, and review of the resulting proof before it is published in its final form. Please note that during the production process errors may be discovered which could affect the content, and all legal disclaimers that apply to the journal pertain.



Lunar polar craters – icy, rough or just sloping?

Vincent R. Eke^{a,*}, Sarah A. Bartram^a, David A. Lane^a, David Smith^a, Luis F. A. Teodoro^b

^a*Institute for Computational Cosmology, Department of Physics, Durham University, Science Laboratories, South Road, Durham DH1 3LE, U.K.*

^b*BAER, Planetary Systems Branch, Space Science and Astrobiology Division, MS: 245-3, NASA Ames Research Center, Moffett Field, CA 94035-1000, U.S.A.*

Abstract

Circular Polarisation Ratio (CPR) mosaics from Mini-SAR on Chandrayaan-1 and Mini-RF on LRO are used to study craters near to the lunar north pole. The look direction of the detectors strongly affects the appearance of the crater CPR maps. Rectifying the mosaics to account for parallax also significantly changes the CPR maps of the crater interiors. It is shown that the CPRs of crater interiors in unrectified maps are biased to larger values than crater exteriors, because of a combination of the effects of parallax and incidence angle. Using the LOLA Digital Elevation Map (DEM), the variation of CPR with angle of incidence has been studied. For fresh craters, $CPR \sim 0.7$ with only a weak dependence on angle of incidence or position interior or just exterior to the crater, consistent with dihedral scattering from blocky surface roughness. For anomalous craters, the CPR interior to the crater increases with both incidence angle and distance from the crater centre. Central crater CPRs are similar to those in the crater exteriors. CPR does not appear to correlate with temperature within craters. Furthermore, the anomalous polar craters have diameter-to-depth ratios that are lower than those of typical polar craters. These results strongly suggest that the high CPR values in anomalous polar craters are not providing evidence of significant volumes of water ice. Rather, anomalous craters are of intermediate age, and maintain sufficiently steep sides that sufficient regolith does not cover all rough surfaces.

Keywords: Moon, surface; Radar observations; Ices

1. Introduction

Knowing the quantity of water ice that is squirreled away in permanently shaded lunar polar cold traps will constrain models of volatile molecule delivery and retention. It is also of interest as a potential resource for future explorers. The seminal work of Watson et al. (1961) introduced the possibility of water ice accumulations in regions so cold, beneath $\sim 110K$, that ice would be stable against sublimation for billions of years. Using the Lunar Prospector Neutron Spectrometer (LPNS), Feldman et al. (1998) showed that there were concentrations of hydrogen at polar latitudes to the 70 cm depths probed by the neutrons. Eke et al. (2009) showed, with a pixon image reconstruction algorithm that sharpened the LPNS hydrogen map, that the excess polar

*Corresponding author

Email address: v.r.eke@durham.ac.uk (Vincent R. Eke)

hydrogen was preferentially concentrated into the permanently shaded regions. However, while suggestive, the level of ~ 1 wt% Water Equivalent Hydrogen (WEH), inferred from the models of Lawrence et al. (2006), was still not sufficiently high to prove that the hydrogen needed to be present as water ice. Only with the LCROSS impactor (Colaprete et al., 2010) did it become clear that water ice did indeed exist, in a small region within Cabeus, at a level of a few per cent by mass within the top metre or two of regolith. The hydrogen maps produced from the LPNS by Teodoro et al. (2010) implied that there may well be significant heterogeneity between permanently shaded polar craters, so the LCROSS result should not be assumed to apply to all of these cold traps.

Infra-red spectroscopy of the sunlit lunar surface has shown not only absorption by surficial water and hydroxyl (Pieters et al., 2009; Clark, 2009), but also that these molecules are mobile across the surface depending upon the time of lunar day (Sunshine et al., 2009). This supports the idea of a lunar “water cycle” of the sort envisaged by Butler (1997) and Crider and Vondrak (2000), but major uncertainties remain in our understanding of the efficiency with which cold traps protect the volatiles that they receive (Crider and Vondrak, 2003).

The Lyman Alpha Mapping Project (LAMP) instrument on LRO has shown, using radiation resulting from distant stars or scattering of the Sun’s Ly α from interplanetary hydrogen atoms, that permanently shaded polar craters typically have a low far-UV albedo (Gladstone et al., 2012). These results are consistent with 1 – 2% water frost in the upper micron of the regolith of the permanently shaded regions, with the observed heterogeneity between different craters perhaps implying a sensitivity to local temperatures. Knowing how heterogeneous the water ice abundance is would provide insight into which physical processes are most relevant for determining volatile retention.

Another widely-used remote sensing technique with the potential to provide information about both the composition and structure of near-surface material is radar (Campbell, 2002). This often involves sensing the polarisation state of the reflected radiation when circularly polarised radio waves are transmitted towards a surface. The dielectric properties of the materials present, surface roughness, including rocks and boulders, composition and size of any buried materials within the regolith and the depth of regolith above bedrock could all affect the returned signal. For 13 cm radiation, the dielectric properties of regolith are such that the upper few metres of the surface can be probed by radar measurements. Given the complex nature of the scattering problem, it can be difficult to know what to infer from radar data without additional insights into the likely surface composition or structure. The most frequently used way of characterising the returned signal is to take the ratio of powers in the same sense (as transmitted) to the opposite sense of circular polarisation, namely the circular polarisation ratio, or CPR. A CPR of zero would be expected for specular reflection from a medium with higher refractive index, whereas higher CPR values can result from multiple scattering, which may imply the presence of a low-loss medium such as water ice making up the regolith.

Radar observations of Europa, Ganymede and Callisto showed surprisingly high CPR values of ~ 1.5 (Campbell et al., 1978; Ostro et al., 1992). The low densities of these satellites were indicative of them having icy compositions. The temptation to associate high CPR values with ice increased when observations of the polar regions of Mercury showed that high CPR regions were associated with permanently shaded craters, within which temperatures could be low enough for water ice to be stable against sublimation (Harmon et al., 1994). Recent results from MESSENGER’s neutron spectrometer (Lawrence et al., 2013) support this conclusion.

It is less clear what should be inferred from radar observations of the Moon about the presence of water ice in permanently shaded craters. The Clementine mission transmitted circularly

81 polarised radio waves into the lunar polar regions, with the reflected flux measured on Earth.
 82 An increase in same-sense polarised power at zero phase angle was interpreted by Nozette et al.
 83 (1996) as possible evidence for constructive interference from waves taking reversed routes in-
 84 volving multiple scattering within an icy regolith. This coherent backscatter opposition effect
 85 (CBOE Hapke, 1990) is one physical process that would produce high CPR values. However,
 86 Stacy et al. (1997), Simpson and Tyler (1999) and Campbell et al. (2006) showed that high CPR
 87 could also result from surfaces that were rough on scales within an order of magnitude in size of
 88 the 13 cm radar wavelength, which would help to explain why at least some of the high CPR re-
 89 gions occurred in clearly sunlit locations where water ice would not exist in significant amounts.

90 In parallel with the acquisition of remote sensing radar data, various models have been con-
 91 structed to help to interpret the CPR measurements. Descriptions of the scattering mechanisms
 92 relevant to the problem are given by Campbell (2002, 2012). An empirical two-component model
 93 was developed by Thompson et al. (2011) with a view to decoding CPR data from the Mini-SAR
 94 and Mini-RF instruments on Chandrayaan-1 and LRO respectively. The most physically moti-
 95 vated modelling to date was carried out by Fa et al. (2011) who used vector radiative transfer
 96 theory to follow the polarisation state of the input electromagnetic radiation. While their model
 97 did not include multiple scattering, so had no CBOE, it did predict the impact of incidence angle,
 98 regolith thickness, buried rocks and surface roughness on the returned signal. They found that
 99 the similarity in dielectric permittivity between ice and a silicate regolith would make it difficult
 100 to identify ice mixed into such a regolith.

101 The wealth of recent information returned from lunar missions provides the possibility of
 102 discriminating between the different reasons for high CPR regions on the lunar surface. Spudis
 103 et al. (2010) used the north pole CPR mosaic from the Mini-SAR instrument on Chandrayaan-1 to
 104 show how fresh craters showed high CPR both inside and out, whereas a set of ‘anomalous’ polar
 105 craters had high interior CPRs without any corresponding enhancement just outside their rims. If
 106 meteorite bombardment removed roughness at a similar rate inside and outside these craters then
 107 this is suggestive that something other than roughness was responsible for the anomalously high
 108 CPRs inside these craters. That something could be water ice. Using Mini-RF data from LRO,
 109 Spudis et al. (2013) argued that the abundance of anomalous craters was much greater near to the
 110 lunar poles than at lower latitudes, with the implication that temperature might be an important
 111 variable in determining the CPR in these craters.

112 More recently, Fa and Cai (2013) studied examples of both polar and non-polar fresh and
 113 anomalous craters using data from the Mini-RF Synthetic Aperture Radar instrument on board
 114 LRO, finding polar and non-polar anomalous craters to have indistinguishable distributions of
 115 pixel CPR. Given that water ice is not the reason for the non-polar crater interiors having anoma-
 116 lously high pixel CPR values, why should it be necessary for the high pixel CPR values in
 117 anomalous polar craters? Furthermore, Fa and Cai (2013) used LROC images to see boulders
 118 within, and not outside, the non-polar anomalous crater. Despite the mismatch in scales between
 119 the $>1\text{-}2$ m-sized rocks and the 13 cm radar wavelength, the model of Fa and Cai (2013) shows
 120 that dihedral scattering from such rocks can still significantly increase the CPR. This provides a
 121 potential reason for the anomalous crater CPR distributions and evidence for some differential
 122 weathering from the crater interior to its exterior. Unfortunately, the lack of illumination into
 123 the floors of the polar craters precluded such a detailed investigation of rockiness being carried
 124 out in these locations. In their detailed study of Shackleton crater, Thomson et al. (2012) found
 125 that “Mini-RF observations indicate a patchy, heterogeneous enhancement in CPR on the crater
 126 walls whose strength decreases with depth toward the crater floor.” While placing an upper limit
 127 of $\sim 5 - 10$ wt% H_2O ice in the uppermost metre of regolith, they conclude that the result “...

128 is most consistent with a roughness effect due to less mature regolith present on the crater wall
129 slopes.”

130 In this paper, the polar craters studied by Spudis et al. (2010) will be investigated using a
131 combination of topography, radar and temperature data sets, with a view to determining what
132 is responsible for the anomalous polar craters, and is anything special about their cold floors.
133 Section 2 contains descriptions of the various data sets that will be employed and the set of polar
134 craters to be studied. Results concerning the variation of CPR with incidence angle and position
135 within the crater, as well as a simple model showing the impact of parallax in the range measure-
136 ment, are contained in Section 3. What these CPR measurements imply about the presence of
137 polar water ice are discussed in Section 4, and conclusions drawn in Section 5.

138 2. Data

139 A number of different lunar data sets, available from the Geosciences Node of NASA’s Plan-
140 etary Data System (PDS¹), will be used. This section describes them briefly, as well as providing
141 details of the set of north polar craters to be studied.

142 2.1. LOLA Topographical data

143 The polar stereographic Lunar Orbiter Laser Altimeter (LOLA) Digital Elevation Map (DEM)
144 for the north pole, with a pixel size of 80 m, is used in this study (Smith et al., 2010). These data
145 are used for finding craters using the algorithm defined in the Appendix, which returns crater
146 locations, diameters (D) and depths (d), and also to determine surface normals and hence radar
147 angles of incidence for the Synthetic Aperture Radar (SAR) observations.

148 2.2. Synthetic Aperture Radar data

149 Both the S-band (12.6 cm wavelength) CPR and reflected power (characterised through the
150 first element of the Stokes vector, S_1) polar stereographic mosaics for the Mini-SAR instrument
151 on Chandrayaan-1 (Spudis et al., 2009) and Mini-RF on LRO (Nozette et al., 2010) are used
152 here. These instruments use a hybrid polarity architecture (Raney, 2007), emitting circularly
153 polarised radio waves and receiving two orthogonal linear polarisations coherently, enabling the
154 Stokes vector of the returned signal to be fully reconstructed. The PDS mosaics of CPR and
155 S_1 provide measurements with a pixel size of 75 m for Mini-SAR and ~ 118 m for Mini-
156 RF down to a latitude of $\sim 70^\circ$. Both of these instruments were side-facing, relative to the
157 direction of spacecraft motion, with Mini-SAR having a nadir angle of $\sim 33^\circ$ and Mini-RF
158 $\sim 48^\circ$. The currently available mosaics are neither controlled, to take into account the imperfect
159 knowledge of the spacecraft trajectory, nor orthorectified to tie the images to an underlying base
160 map such as that provided by the LOLA DEM. Orthorectification involves removing distortions
161 in the inferred range distance, perpendicular to the direction of spacecraft motion, resulting from
162 height variations in the topography affecting the return times of the radar pulses (Kirk et al., 2013;
163 Campbell, 2002). The impact of this radar parallax effect is significant and will be considered in
164 detail in this paper. These factors mean that the Mini-SAR and Mini-RF mosaics can be spatially
165 offset from the base map set by the LOLA DEM by up to ~ 5 km and ~ 2 km respectively. The
166 Mini-RF mosaic is a mixture of left- and right-looking measurements, with most pixels being

¹<http://pds-geosciences.wustl.edu>

167 assigned the latest right-looking observation, with $\sim 5\%$ of pixels being left-looking (R. Kirk,
168 private communication). Consequently, the Mini-RF mosaic will not be used for the quantitative
169 analysis towards the end of this paper. It should be noted that near to the poles, right-looking
170 does not imply east-looking. For instance, when the detector is at the north pole, right-looking
171 corresponds to facing south.

172 2.3. Diviner data

173 The Diviner infra-red radiometer on board LRO has measured fluxes from the lunar surface
174 in nine different spectral bands, allowing surface temperatures to be inferred. From these data,
175 with a model to account for the variation in solar illumination over time, maps of average and
176 maximum temperatures can be calculated (Paige et al., 2010). Given the exponential dependence
177 of both water molecule diffusion and sublimation rates on temperature, the map of maximum
178 temperature is likely to be most relevant to the distribution of polar water ice and is used here.
179 These T_{\max} values are provided in a set of triangular pixels poleward of 75° latitude, with a
180 spatial resolution of ~ 500 m.

181 2.4. The crater set

182 A set of polar craters was found by applying the algorithm described in the Appendix to the
183 LOLA 80 m north pole stereographic DEM. Briefly, this method involves finding depressions
184 in the surface by tracking to where ‘water’, placed uniformly across the surface, runs. Isolated
185 ‘puddles’ provide possible candidates for simple, isolated craters that do not have significant
186 sub-cratering. A crater-shaped filter is run over the DEM in the vicinity of sufficiently isolated
187 depressions. This filter picks out circularly symmetric concave regions with a circular convex
188 rim. The best match of the crater-shaped filter with the DEM defines the crater centre and radius,
189 r_c , and the value of the filtered DEM provides a quantitative measure of how crater-like each
190 candidate is.

191 42 of the craters studied by Spudis et al. (2010) were matched to crater candidates in the
192 LOLA DEM. Locations and radii are provided in Table 1 for this set. Note that, because the
193 Mini-SAR and Mini-RF mosaics have not been orthorectified to the LOLA base map, there are
194 different crater centres for each of these data sets. To determine the crater centres, their radii
195 and approximate locations are taken from the crater-finding algorithm. The radar data are then
196 visually aligned, matching the pattern of nearby craters in the LOLA DEM to those visible in
197 the CPR and S_1 maps. In the radar data, anomalous and fresh craters show up as regions of high
198 CPR, with arcs of high S_1 on the far crater walls. The accuracy with which this alignment can be
199 used to estimate the positions of the crater rims is approximately 2 pixels, which is 150 m for the
200 Mini-SAR data. This is less than 10% of the crater radius for almost all of the craters considered
201 here. Having aligned the rims of the craters in this way, the pre-rectification centre locations are
202 assumed to have the same uncertainty in position. A few of the craters studied by Spudis et al.
203 (2010) are not included in the sample of 42 craters, either because they could not be confidently
204 found in the CPR maps, or because their CPR and S_1 distributions did not allow a clear centre to
205 be inferred.

206 Figure 1 shows probability distributions for pixel CPR values measured from the Mini-SAR
207 mosaic for the interiors and exteriors of all 42 craters. Craters 1 – 33 represent the “anomalous”
208 ones with exterior CPR values being typically lower than interior ones, whereas numbers 34 – 42
209 are fresh craters. For reference, crater 2 is the anomalous crater shown in figure 3 of Spudis et al.
210 (2010).

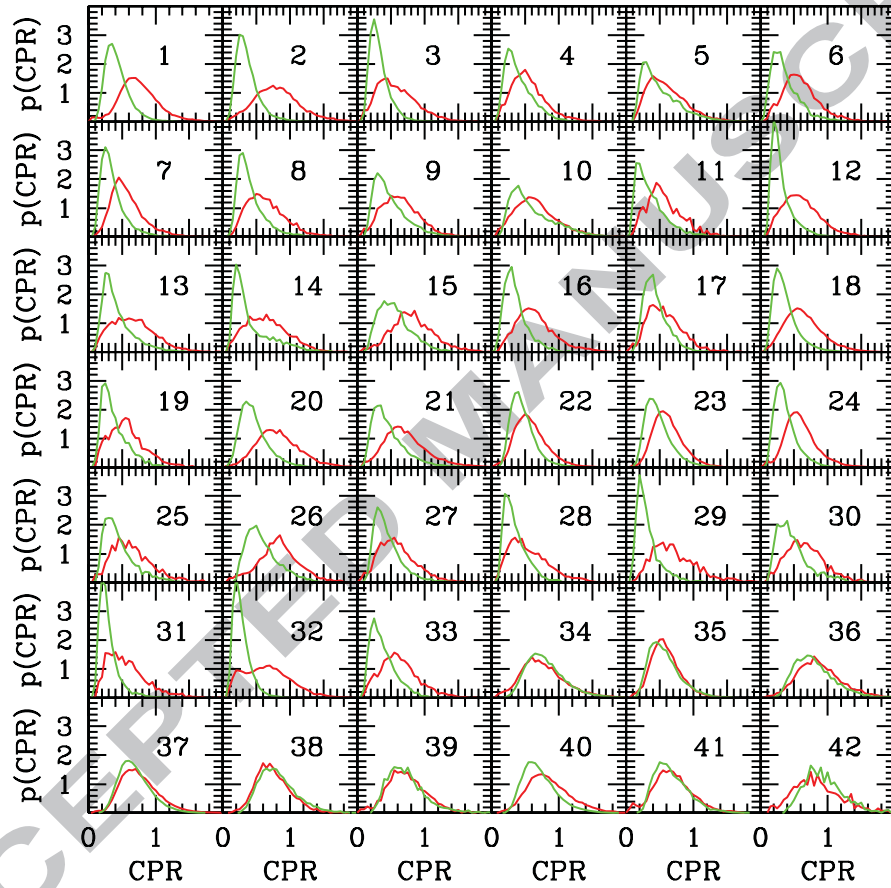


Figure 1: The distributions of pixel CPR for the 42 craters considered, measured from the unrectified Mini-SAR mosaic. Pixels interior to the crater are shown in red and those with radii satisfying $1 < r/r_c < 1.5$ are shown in green. The anomalous craters (numbers 1-33) have significantly different interior and exterior pixel CPR distributions, with the interior distribution skewed to higher values than is seen from regions just outside the crater rim. The fresh craters (numbers 34-42) have very similar interior and exterior CPR distributions.

Table 1: Radii and locations for craters used in this study. Longitudes and latitudes are given in degrees. Different locations are used for the two radar data sets on account of the available mosaics not having been tied to the LOLA base map. Uncertainties on the locations are ~ 80 m, ~ 150 m and ~ 250 m for LOLA, Mini-SAR and Mini-RF respectively.

Crater #	Radius r_c /km	LOLA (lat, lon)	Mini-SAR (lat, lon)	Mini-RF (lat, lon)
1	6.0	79.04, -148.4	78.89, -149.0	78.98, -148.4
2	4.3	84.05, -156.4	83.88, -157.4	84.02, -156.5
3	3.2	80.17, -124.6	80.07, -124.7	80.13, -124.7
4	3.8	80.45, -122.6	80.33, -122.9	80.41, -122.8
5	3.6	85.78, 25.2	85.68, 25.4	85.73, 24.9
6	2.9	85.75, 43.6	85.69, 44.7	85.72, 43.5
7	5.3	86.99, 28.6	87.08, 30.1	86.94, 28.2
8	2.7	88.08, 39.9	88.10, 43.9	88.05, 40.6
9	3.4	87.73, 16.9	87.66, 19.0	87.74, 15.7
10	2.9	87.97, 29.9	88.21, 29.4	87.97, 28.2
11	1.7	89.13, 59.5	89.09, 69.8	89.10, 60.9
12	3.3	88.19, 63.4	88.20, 67.4	88.15, 63.5
13	2.8	86.59, 93.2	86.47, 93.6	86.56, 92.6
14	2.5	88.75, 47.1	88.69, 52.3	88.72, 48.0
15	1.9	81.80, -110.0	81.65, -111.1	81.75, -110.0
16	2.4	82.67, -83.6	82.53, -84.6	82.62, -83.7
17	2.0	82.75, -80.8	82.62, -81.9	82.70, -80.9
18	8.7	80.26, -50.1	80.19, -50.3	80.22, -50.2
19	1.9	86.31, -89.1	86.17, -90.1	86.27, -89.4
20	4.1	87.14, -86.3	86.99, -87.4	87.17, -86.1
21	4.8	81.65, -23.9	81.58, -24.1	81.59, -23.9
22	3.8	85.14, -166.7	84.97, -167.9	85.11, -166.8
23	9.6	87.98, -52.2	87.91, -52.7	88.00, -51.7
24	5.3	83.75, -13.8	83.67, -14.4	83.71, -14.0
25	2.0	86.19, -177.5	86.01, -178.8	86.14, -177.6
26	2.8	86.81, -13.9	86.72, -14.4	86.77, -14.6
27	2.5	84.99, -2.0	84.90, -2.7	84.95, -2.2
28	2.4	87.83, 113.0	87.67, 111.1	87.81, 112.3
29	1.8	86.81, 116.1	86.80, 118.5	86.78, 115.4
30	1.8	85.93, 111.7	85.80, 111.4	85.90, 111.3
31	1.5	85.43, 105.3	85.32, 105.3	85.40, 105.0
32	5.4	81.15, 137.7	81.22, 138.3	81.12, 137.6
33	2.3	82.12, 92.3	81.99, 91.7	82.09, 92.1
34	6.5	81.45, 22.6	81.35, 22.6	81.40, 22.9
35	4.7	84.86, 35.6	84.76, 35.7	84.81, 35.5
36	2.3	87.69, 30.8	87.74, 33.9	87.68, 29.6
37	9.8	82.42, -68.7	82.32, -68.7	82.38, -68.8
38	2.7	84.48, -132.4	84.34, -133.1	84.44, -132.3
39	1.6	81.62, -161.7	81.51, -161.4	81.58, -161.7
40	6.4	84.82, -172.2	84.67, -173.0	84.79, -172.4
41	2.8	80.93, 117.1	80.82, 117.4	80.88, 117.0
42	1.2	86.16, 71.0	86.06, 71.6	86.12, 70.7

211 3. Results

212 The different CPR distributions for pixels interior and exterior to the polar anomalous craters
213 are clearly seen in Figure 1. This section contains the results from a more detailed analysis of
214 what gives rise to these differences.

215 3.1. Stacking craters

216 If the anomalously high interior CPR measurements in polar craters were the result of sig-
217 nificant deposits of water ice, then one might expect to see a variation of CPR with the posi-
218 tion within the crater, reflecting varying insolation, temperature and hence water ice stability
219 (Vasavada et al., 1999). To enhance the signal-to-noise, all 33 anomalous craters have been
220 stacked together to produce the Mini-SAR CPR map shown in Figure 2. The stacking process
221 involves dividing each pixel's CPR by the mean crater interior CPR and the distance from the
222 centre is expressed as a fraction of the distance to the crater's edge. The map for each crater is
223 rotated to have the north pole at the top, and the final stacked map is the mean of these processed
224 crater maps. It is apparent from the figure that the highest CPR is typically on the poleward side
225 of the crater, with a distinctive horseshoe pattern of higher CPR around the crater walls.

226 Stacking the same 33 anomalous craters together using the Mini-RF mosaic gives rise to the
227 CPR map in Figure 3. Once again a horseshoe-shaped high CPR region is seen, only in a different
228 part of the stacked crater. Given that the lunar surface will not have changed significantly during
229 the period between Mini-SAR and Mini-RF data collection, it can be inferred that this difference
230 reflects a change in the viewing geometry, as anticipated by the model of Fa et al. (2011) (see
231 their figure 13).

232 This conclusion is strengthened by the corresponding stacked maps of the returned power
233 shown in Figures 4 and 5, which are determined from the S_1 mosaics. Higher returned power
234 suggests the transmitted radiation is nearer to normal incidence on the surface. Consequently,
235 there will be greater specular reflection and a lower returned CPR. Thus, the highly reflective
236 parts of the stacked returned power maps correspond to the low parts in the CPR maps. When
237 the surface is viewed at larger angles of incidence, the multiply scattered radiation becomes
238 increasingly important and the returned CPR increases while the returned power decreases. The
239 stacked crater maps shown in these figures all have north to the top, but the radar look direction
240 does not always have the same bearing because the side-facing detector will change its look
241 direction near to the pole. In addition to having different look directions for the different craters
242 contributing to the stacked map, the incidence angle in any given pixel will vary between craters
243 as they have a variety of diameter-to-depth ratios. Consequently, these stacked maps are for
244 illustrative purposes only, and all subsequent radar results treat the craters individually, using
245 a look direction inferred by determining the position of the maximum reflected power in that
246 crater's S_1 map.

247 From these figures, it is clear that the largest factor affecting the CPR maps of these polar
248 craters is the angle of incidence of the observations. As the Mini-RF mosaic includes both left
249 and right-looking measurements it will not be possible to infer an appropriate, reliable single
250 crater look direction from the mosaic, so attention will now be focussed onto the Mini-SAR data.

251 3.2. Slopes and parallax

252 Given that the angle of incidence is a complicating, and for the purposes of learning about the
253 lunar surface uninteresting, factor driving the CPR distribution within the polar craters, it would
254 be good to remove its effect. While there have been models of how CPR varies with angle of

incidence (Thompson et al., 2011; Fa et al., 2011), a more robust approach involves determining the dependence using the data themselves.

Each crater has an S_1 map with a high spot that should be nearest to normal incidence for the incoming radar. This is defined within a cone of opening angle 20° from the centre of the crater, and is used to define the azimuthal look direction of the detector appropriate to this particular crater. In combination with the nadir angle of the detector, this provides a vector for the incoming radiation. Finite differencing methods applied to the LOLA DEM provide a local surface normal. The scalar product of these unit vectors yields the cosine of the angle of incidence for each pixel in each of the craters being considered. In this way, each pixel CPR can be mapped to a corresponding angle of incidence.

One final, but crucial, complication is to determine to which bit of the surface does an unrectified Mini-SAR mosaic pixel correspond. The effect of parallax in radar range measurements distorts the inferred pixel position because the mapping of return signal time to distance should account for variations in the height of the surface being mapped (Campbell, 2002). As the Mini-SAR crater positions have been individually chosen such that the crater rims appear to line up correctly (something that the stacked CPR and S_1 mosaics imply has been done reasonably well), the mean altitude of the crater rim is set as the reference height. All other points within $1.5r_c$ of the crater centre are then shifted a distance p away from the detector in the range direction using

$$\Delta h = p \tan \alpha, \quad (1)$$

where Δh represents the change in height, at the shifted position, relative to the reference height, p is the parallax, and α is the angle of incidence of the radar (see section 4.11 in Campbell, 2002). An iterative procedure is necessary because the parallax displacements depend upon the topography at to-be-determined positions in the DEM. This shift moves unrectified pixels within the crater having $\Delta h < 0$ to positions that are nearer to the detector (i.e. $p < 0$). As a consequence, equally spaced pixels in the distorted, unrectified map preferentially sample the near crater wall at higher angles of incidence.

Having determined which part of the LOLA DEM should be matched to each pixel in the vicinities of the craters being considered, the dependence of pixel CPR on the angle of incidence can be determined. Figure 6 shows the median dependence of the pixel values for each of the 33 anomalous north pole craters being considered here. The median of these curves is shown with the bold black line, which can be well described by the linear fit

$$CPR(\theta) = 0.27 + 0.68(\theta/90^\circ) \quad (2)$$

where θ represents the angle of incidence in degrees. The crater interior shows a strong trend of increasing CPR with increasing angle of incidence, although the individual crater values have a non-negligible scatter about this median relation. A bold green line traces the median dependence for the 33 crater exterior regions out to $1.5r_c$, and clearly shows lower CPR values for intermediate angles of incidence than are typical inside these craters. While the exterior CPR does become more similar to the interior crater values at high and low angles of incidence, it is possible that this is a consequence of inaccuracies in defining the crater edges in the Mini-SAR mosaic.

This measurement of the variation of CPR with angle of incidence could contain dependencies on hidden surface properties that have not been considered, but it serves as a useful starting point for constructing a simple model with which to investigate just how important the

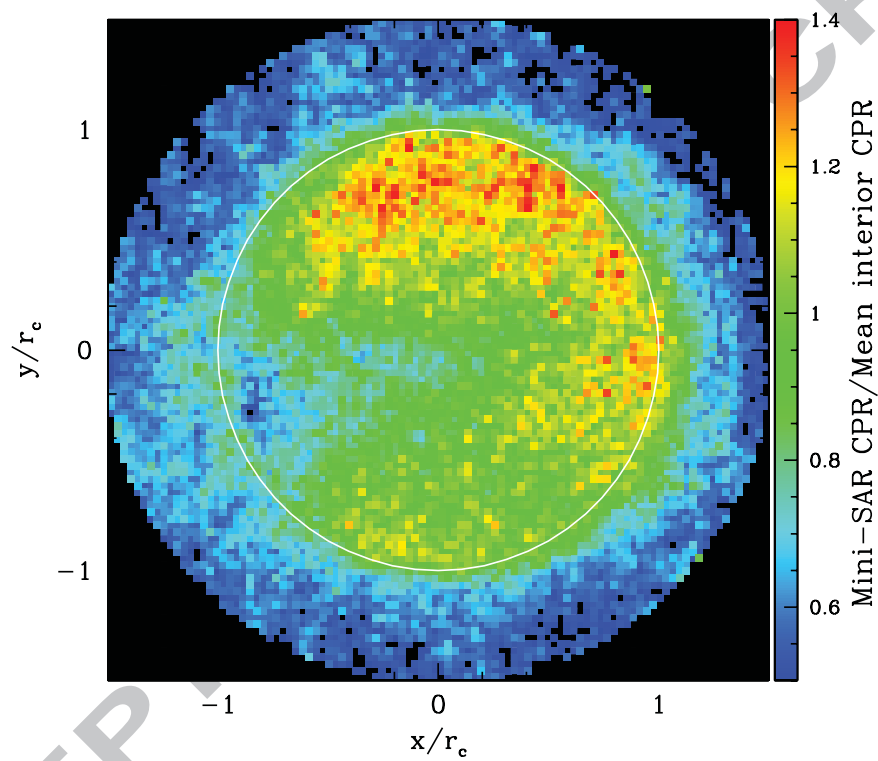


Figure 2: The stacked relative CPR map for the 33 anomalous craters. Each crater map is divided by the mean pixel CPR interior to the crater and rotated to have north at the top before they are stacked together. The white circle represents the edge of the craters contributing to the average.

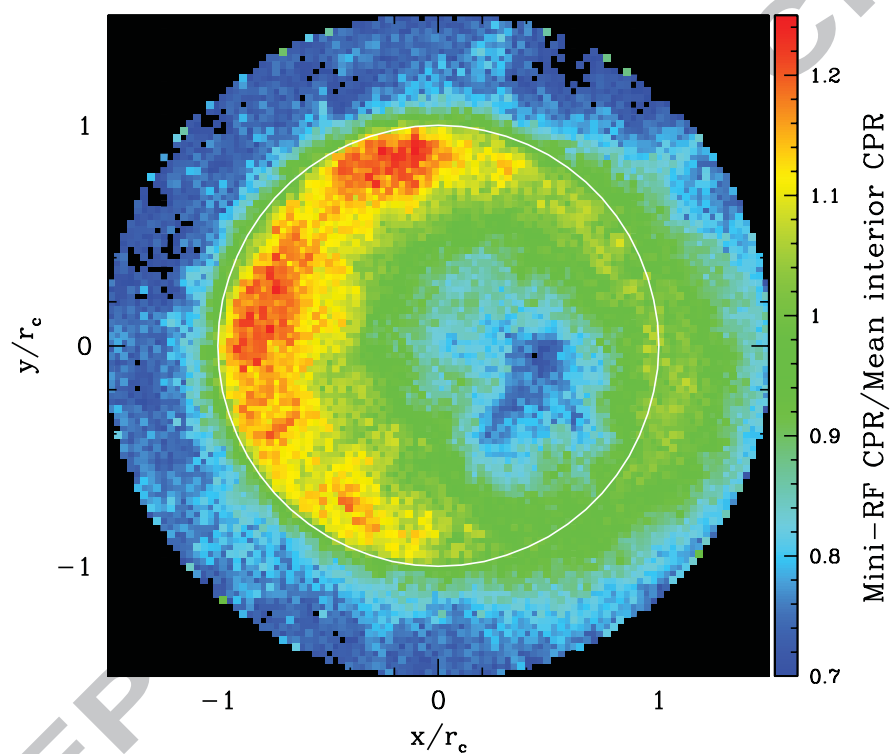


Figure 3: The stack of the 33 anomalous crater relative CPR maps using the LRO Mini-RF unrectified mosaic.

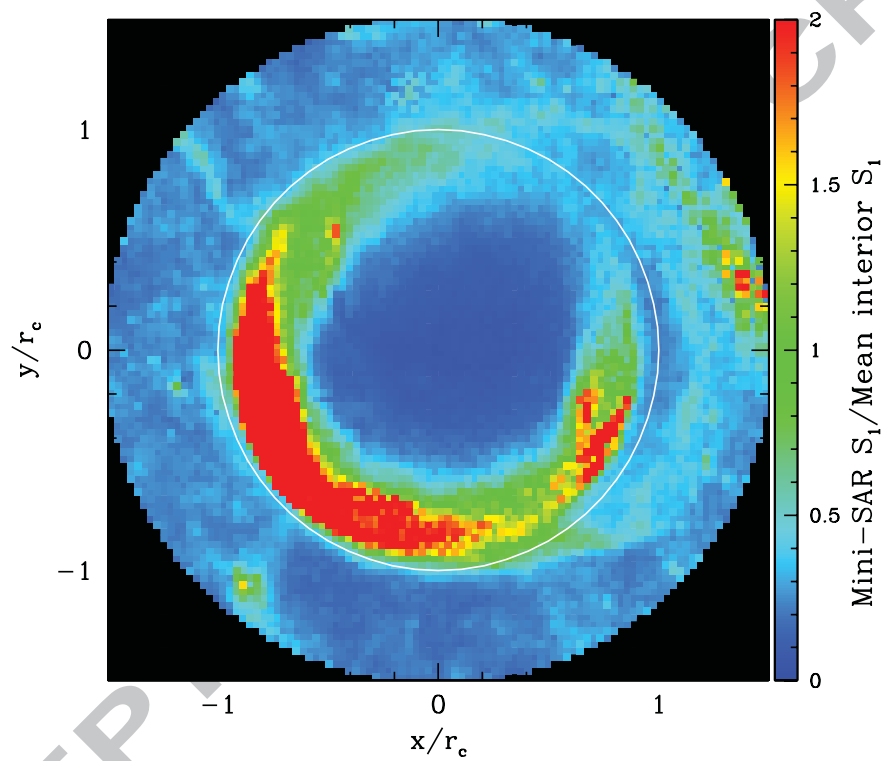


Figure 4: The stacked relative returned power, represented by the first element of the Stokes vector, S_1 , for observations of the 33 anomalous craters made by Mini-SAR. All craters are aligned so that north points to the top of the image before stacking.

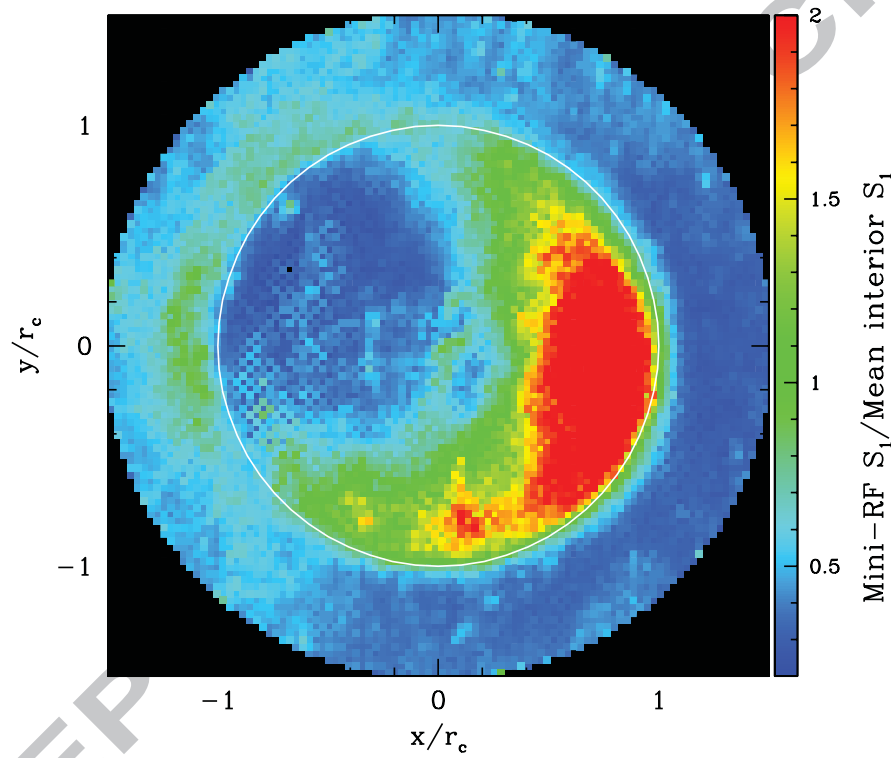


Figure 5: The equivalent of Fig. 4 for the LRO Mini-RF S_1 mosaic.

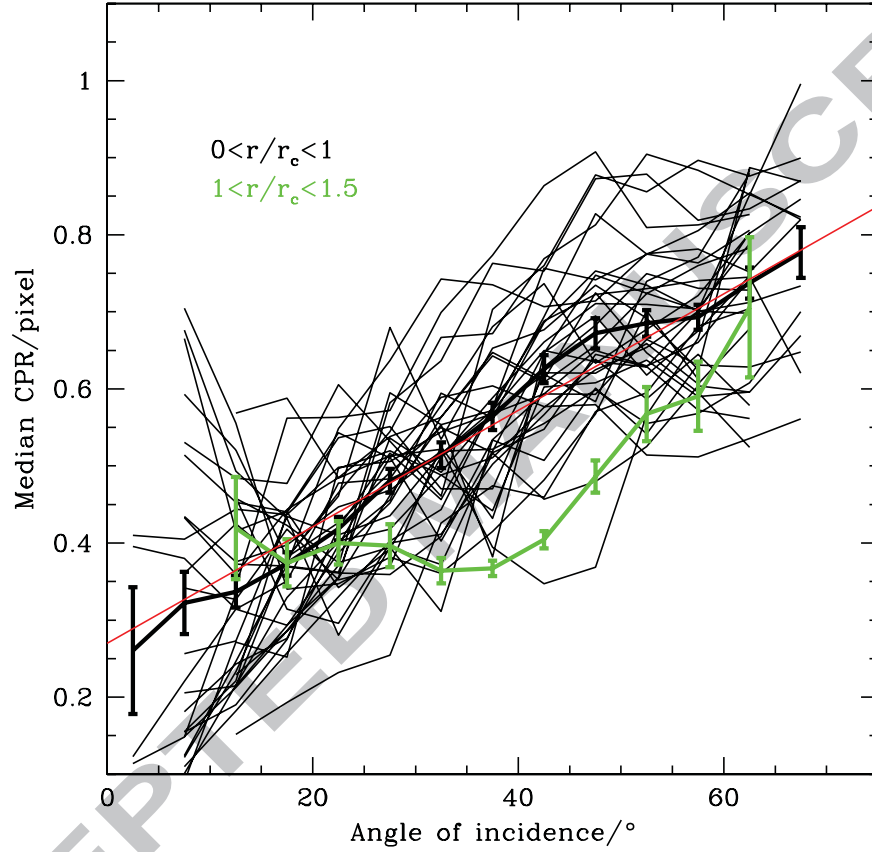


Figure 6: The variation of median CPR as a function of angle of incidence between the incident radar and the surface normal for the 33 anomalous craters. The light black lines show the individual crater median pixel CPR curves, and the heavy black line is the median of these values. Error bars show an estimate of the statistical uncertainty on the inferred median based on the 16th and 84th percentiles of the distribution of CPR values from the individual craters at each angle of incidence and the assumption that this distribution is Gaussian. The heavy green line is the median over all craters for the crater exterior out to $1.5r_c$. Positions have been rectified to account for the parallax prior to determining into which radial range they fall. The red line shows a straight line fit to the median interior CPR relation.

rectification process is. A model crater was created with diameter $2r_c = 6$ km, and a diameter-to-depth ratio of 5.5, typical of the anomalous polar craters considered here. The radial height profile, $a(x)$, with $x = r/r_c$ being the radius in terms of the crater radius, was defined via $y(x) = a(x)/r_c$, where

$$y(x) = \begin{cases} y_0 + \eta x^2 & \text{if } x \leq x_1, \\ y_1 + y'_1(x - x_1) & \text{if } x_1 \leq x \leq x_2, \\ y_2 + \beta[(x_2 - 1)^2 - (x - 1)^2] & \text{if } x_2 \leq x \leq x_3, \\ y_3 + \gamma[(x - x_4)^2 - (x_3 - x_4)^2] & \text{if } x_3 \leq x \leq x_4, \\ y_4 & \text{if } x_4 \leq x. \end{cases} \quad (3)$$

y_0 represents the central depth divided by the crater radius, which is just twice the reciprocal of the diameter-to-depth ratio, while y_n for $n > 0$ is the value of y evaluated at x_n . y'_1 denotes dy/dx evaluated at x_1 . With the outer boundary condition set as $y_4 = -0.04$ at $x_4 = 1.5$ and the two inner curvatures chosen to be $\eta = 1$ and $\beta = 2$, the requirements that the function is continuous and differentiable sets the remaining constants via

$$x_1 = \frac{1 - \sqrt{1 - \frac{y_0}{\eta}(1 + \eta/\beta)}}{1 + \eta/\beta} \quad (4)$$

$$x_2 = 1 - \frac{\eta}{\beta} x_1 \quad (5)$$

$$x_3 = 1 - \frac{y_4}{\beta(x_4 - 1)} \quad (6)$$

$$\gamma = \frac{\beta(x_3 - 1)}{x_4 - x_3}. \quad (7)$$

This cross-section for the model crater is shown in Figure A.17 and has a maximum smooth slope for the crater wall of $\tan^{-1} y'_1 \approx 23^\circ$. A regular 75 m grid of pixels was created out to $x_4 = 1.5$ from the crater centre. Assuming that these pixels were unrectified, the corresponding rectified positions in the crater were calculated, the angles of incidence to the nominal detector with a nadir angle of 33° were inferred and CPR values were assigned according to equation (2).

The resulting unrectified CPR mosaic is shown in Figure 7 from which it can be seen that the high CPR values associated with the near wall, viewed at large angles of incidence, occupy a significantly larger fraction of the crater interior pixels than the more nearly normal incidence parts of the far wall. Figure 8 shows the same pixels shifted to the parts of the crater that they actually sample. With the effect of parallax removed from the map, it becomes apparent just how the pixels are biased to measure the CPR of the near wall of the crater. Even with 75 m unrectified resolution of a 6 km diameter crater, there are significant parts of the far wall that are completely unsampled.

The impact of this uneven sampling of the crater on the probability distribution of pixel CPR values is shown in Figure 9. Dashed red and green lines show how the interior and exterior pixel CPR distributions can look significantly different, despite both being drawn from an identical relation for CPR as a function of angle of incidence. The peak of the distribution shifts from a CPR of ~ 0.5 to ~ 0.7 , as a result only of the bias caused by using a mosaic uncorrected for the effect of parallax and the dependence of CPR on angle of incidence. These pixel CPR distributions are much more sharply peaked than those in Figure 1 that were measured for real craters using the Mini-SAR mosaic. One way in which the distribution would be broadened

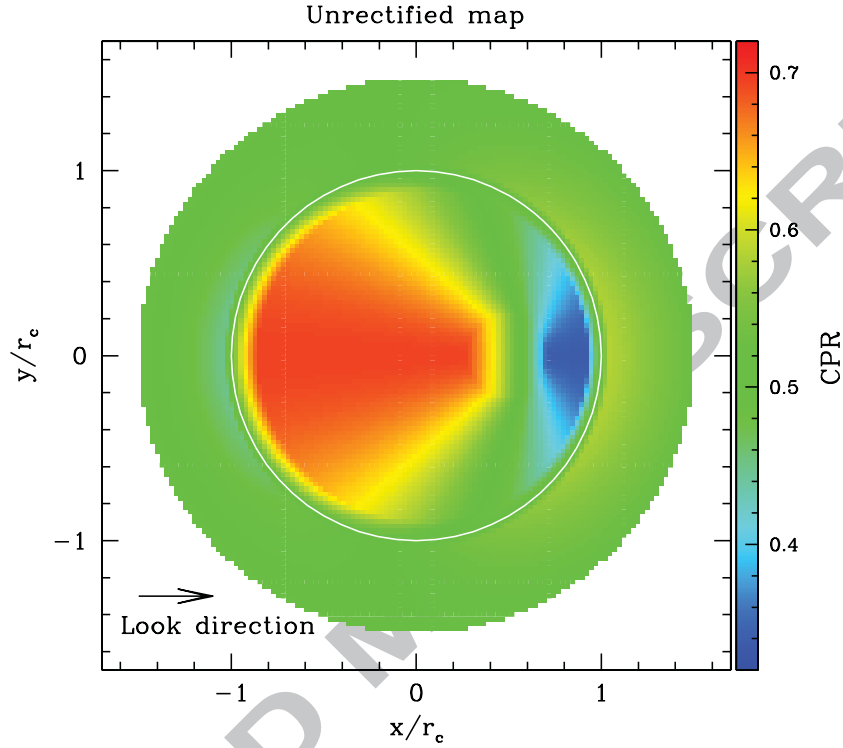


Figure 7: An unrectified CPR mosaic of a model crater with $r_c = 3\text{km}$, a diameter-to-depth ratio of 5.5 and a rim height of $0.04r_c$. The model SAR is looking from the left with a look angle of 33° and the mosaic has 75m square pixels.

would be if there were significant statistical uncertainties on the measurements. The solid lines in Figure 9 show that including a 40% scatter in the assumed CPR at any particular angle of incidence produces distributions that look not unlike those from a few of the anomalous craters. Is it reasonable that such large observational uncertainties exist? This can be indirectly addressed by considering the variation in CPR between adjacent pixels in the Mini-SAR mosaic. The root mean square fractional difference in CPR varies only slightly across the whole polar region, and typically has a value of 25 – 30% in the vicinity of the craters studied here. This represents an upper limit on the size of the statistical uncertainties in the mosaic CPR values, because some of these variations on small scales are presumably the result of varying surface properties. Thus, it can be safely concluded that observational uncertainties in conjunction with slopes and the bias introduced by parallax are not sufficient to explain the measurements. This implies that there must be some additional process responsible for changing the CPR in a sys-

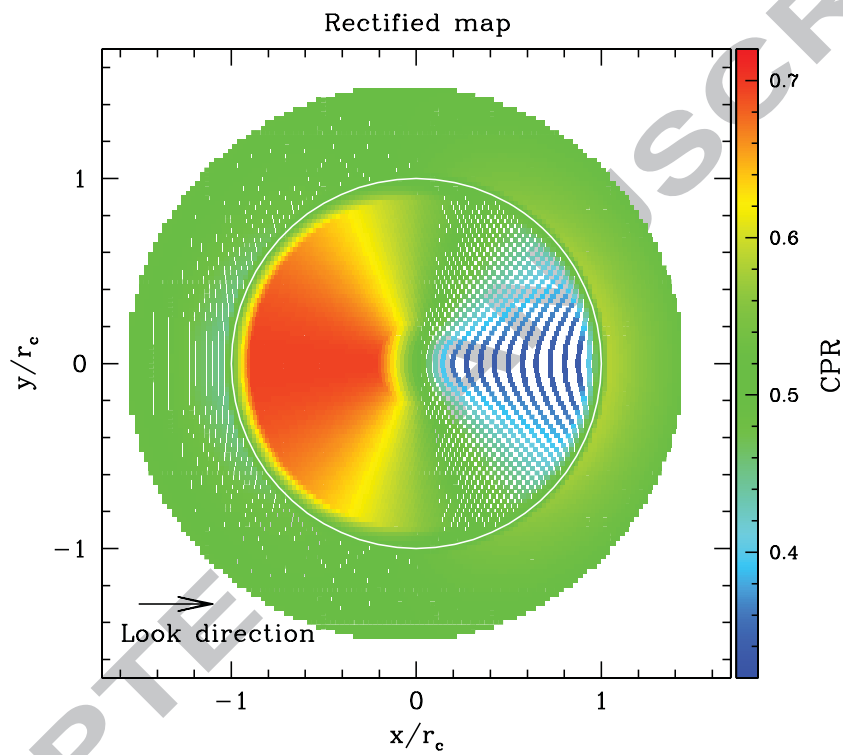


Figure 8: The rectified version of Fig. 7, with each coloured point showing the true position within the crater that it samples. White regions show parts of the crater into which none of the unrectified mosaic pixels are mapped when the parallax correction moves pixels beneath the crater rim toward the detector. The colour relates directly to the angle of incidence at which the surface is viewed through equation (2).

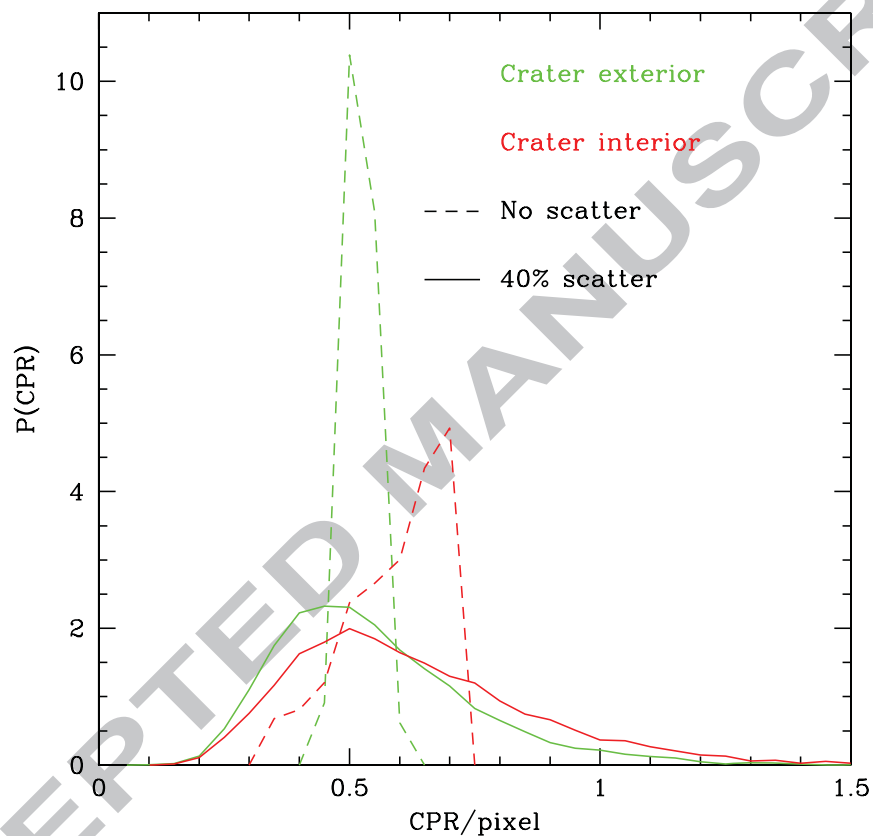


Figure 9: The distribution of pixel CPR values for the interior (red) and exterior (green) of the model crater. Dashed lines show results when no scatter is added in the model CPR value at a given angle of incidence, whereas the solid lines show the effect of including a 40% 1σ Gaussian scatter around the median value.

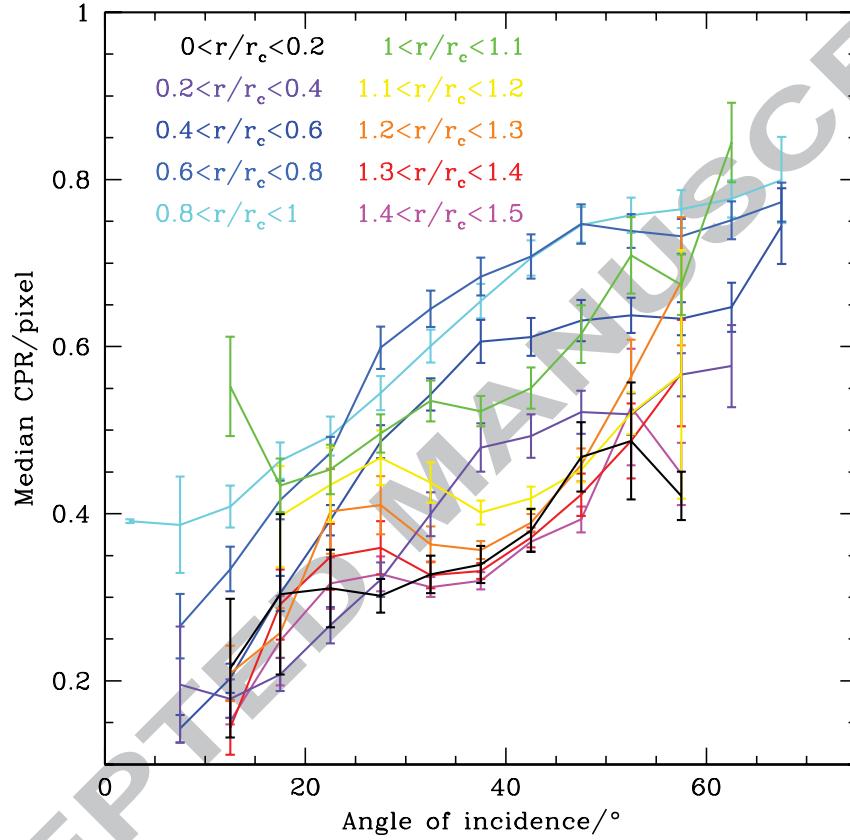


Figure 10: The variation of median CPR as a function of angle of incidence between the incident radar and the surface normal for the 33 anomalous craters. Values show the median of the individual crater values that contribute to each increment of incidence angle. Error bars show an estimate of the statistical uncertainty on the inferred median based on the 16th and 84th percentiles of the distribution of CPR values from the individual craters at each angle of incidence and the assumption that this distribution is Gaussian. The different colours represent different radial ranges of pixels. Positions have been rectified to account for the parallax prior to determining into which radial range they fall.

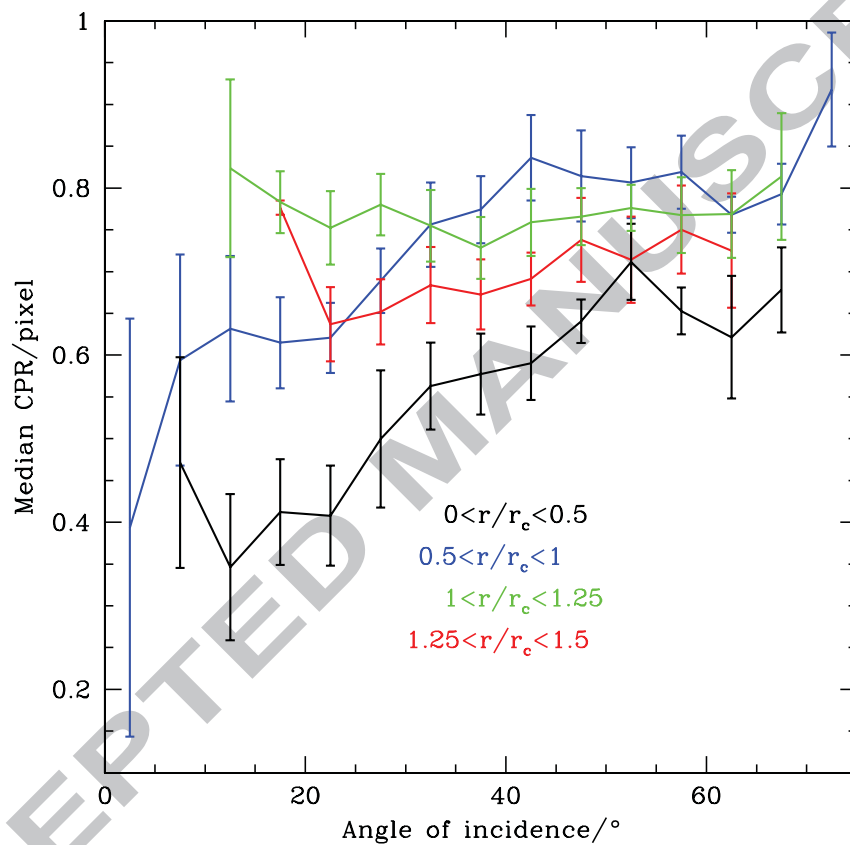


Figure 11: The equivalent of Fig. 10 for the 9 fresh craters. Wider radial ranges are used to suppress statistical noise in the median CPR estimates.

tematic way and that the interior surfaces of these polar anomalous craters are typically different from their exteriors in more complicated ways than merely having steeper slopes.

3.3. The radial variation of CPR

Having determined that the angle of incidence is not solely responsible for the differences between anomalous crater interiors and exteriors, the challenge shifts to trying to determine what other factors are affecting the CPR. Figure 10 shows how the median pixel CPR varies with angle of incidence for different radial ranges both inside and outside the anomalous craters. The pixels are placed into the different radial bins based on their rectified positions within the crater. For all different radial ranges the shape of the median CPR variation with angle of incidence is similar. Only the amplitude changes with radius. The central region of the typical crater has CPR values that are indistinguishable from those of pixels in the crater exterior with $1.2 < r/r_c < 1.5$. Out to $r/r_c \sim 0.8$, the CPR at a given angle of incidence increases systematically with increasing radius. Inaccuracies in determining the precise crater locations may scramble any trends at radii around r_c , but there is a sharper drop in the CPR outside the crater edge than is seen inside the crater. No difference is seen in the results shown in Figure 10 when the anomalous crater sample is split in half either by crater radius or latitude. The increased CPR at any given angle of incidence seems to increase with increasing local slope. At radii satisfying $0.5 \lesssim r/r_c \lesssim 1$, where the CPR is largest for a given angle of incidence, the azimuthally-averaged slopes are typically $\sim 25^\circ$. However, the inaccuracy in the alignment of CPR and DEM maps and the relatively poor spatial resolution preclude a more detailed comparison of CPR with local slope at present.

The corresponding results for the 9 fresh craters are shown in Figure 11. Wider bins in radius are used to prevent the results becoming too noisy given the relatively small number of fresh craters. The variation of CPR with angle of incidence is much weaker than for the anomalous craters. Also, the radial variation, while qualitatively similar to that seen for the anomalous craters, is less pronounced. This is consistent with what one might expect from a surface containing a uniform scattering of blocky ejecta behaving like corner reflectors.

Maps of the variation of CPR relative to the typical value at each incidence angle in each crater are shown in Figure 12. Although the maps are quite heterogeneous, the relatively low CPR values tend to be either in the crater centres or on the far wall as viewed by the detector. Arrows show the direction in which each crater is viewed, as determined from the high spots in the individual crater S_1 maps. Relatively high CPR values tend to be concentrated onto the crater walls. The median CPR values as a function of incidence angle are determined from rectified pixels satisfying $r/r_c < 0.8$. This is done to prevent errors arising from misalignments between the Mini-SAR mosaic and the LOLA DEM. Near to the crater rim, the slopes change rapidly, such that any misalignments between data sets would lead to pixels being assigned very wrong incidence angles, biasing the inferred CPR as a function of incidence angle. This effect may be behind the slightly non-monotonic behaviour noted in Figure 10 for the radial bins adjacent to the rim.

Figure 13 is included to help the interpretation of the relative CPR maps in Figure 12. It shows how the angle of incidence varies with position within the model crater used in Section 3.2, and is effectively just a rescaled version of Figure 8. The comparison of local CPR with that at comparable angles of incidence, given in Figure 12 within each crater, is showing along a line of constant colour in Figure 13, with the orientation set by the azimuthal look direction, where are the higher and lower values of CPR.

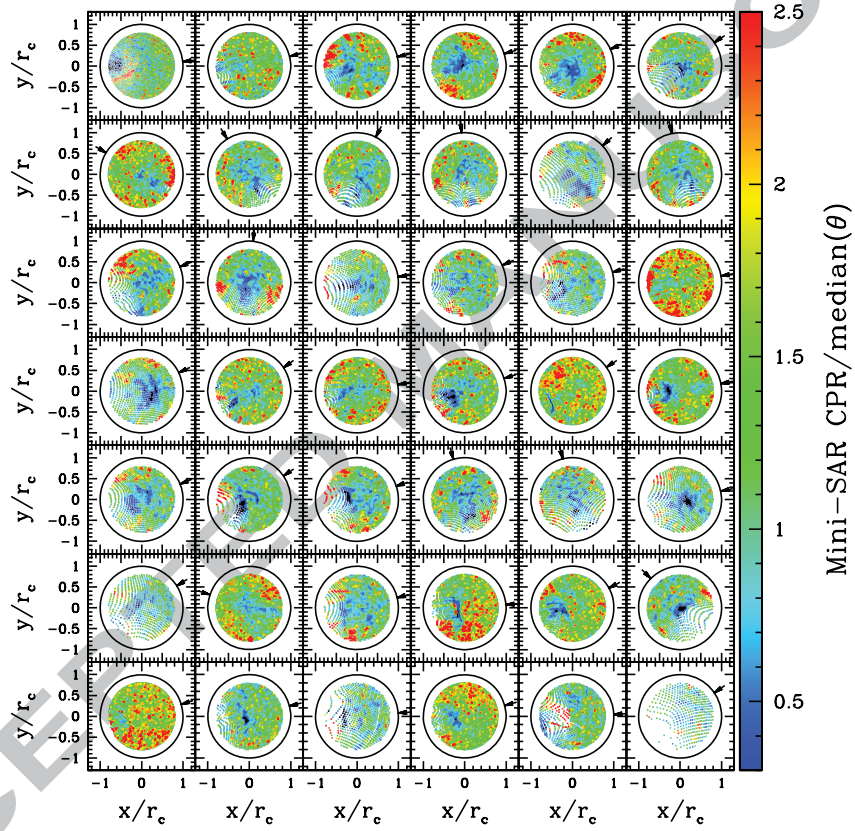


Figure 12: Maps of Mini-SAR CPR/median CPR at that incidence angle for each of the 42 craters. The craters are ordered as in Figure 1 and the pixels are plotted at their rectified locations, with north to the top. Median CPR as a function of incidence angle is calculated for each of the craters individually, using only the pixels with rectified radii having $r/r_c < 0.8$. Black arrows show the azimuthal look direction inferred from the S_1 mosaic for each crater.

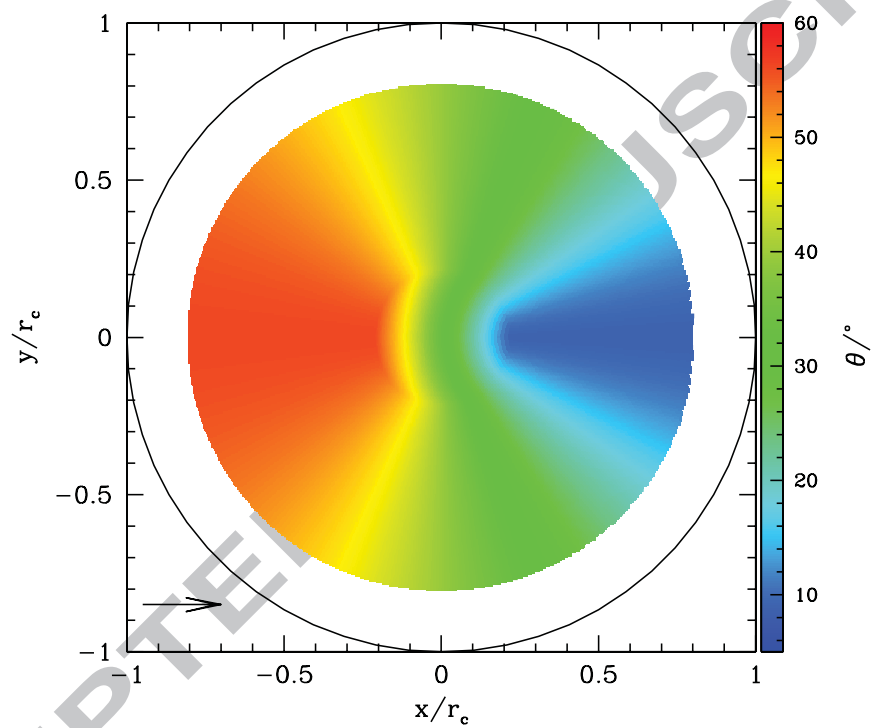


Figure 13: The distribution of incidence angle for the model crater considered in Section 3.2. This shows which parts of a typical crater are viewed at the same angle of incidence, and represents a remapped version of Fig. 8. The detector is looking along the $+x$ direction at the model crater, as shown by the black arrow.

383 4. Implications for the detection of water ice

384 The results in the previous section showed that high CPR regions within polar anomalous
385 craters, once angle of incidence effects are removed to the extent that is possible with the data
386 sets being used here, tend to be found on the steep crater walls. This finding matches that
387 of Thomson et al. (2012) from their detailed study of Shackleton crater. Figure 14 shows the
388 stacked map of the maximum temperature, T_{\max} , relative to the mean maximum temperature
389 within each crater, inferred from Diviner measurements for the 33 anomalous craters. For all
390 craters, the largest interior T_{\max} values exceed 290K and are found on the equator-facing walls,
391 where direct sunlight can occasionally be seen. The stacked pole-facing slope and crater floor
392 have the lowest maximum temperatures, typically 70K but ranging from 30 – 130K, because
393 they only ever receive reflected sunlight. Given that surficial water ice should be stable against
394 sublimation for temperatures beneath ~ 100 K, one might well expect any water ice to be located
395 in these relatively cold regions within the craters. This pattern of maximum temperatures is
396 similar to that seen in the average temperatures, and neither of them reflect the variation of CPR,
397 as might be expected if significant deposits of water ice were responsible for the elevated interior
398 CPRs in the anomalous polar craters.

399 It is possible that water ice could be insulated by a layer of mantling regolith, in which
400 case the CPR variations within anomalous craters might not be expected to reflect those in the
401 temperature. Perhaps the central regions of craters are covered by too much regolith for the
402 radar to see underlying water ice. In contrast, the steep crater sides should not be covered by
403 deep regolith. However, in these regions, the CPR variations still do not reflect the variations in
404 temperature determined using Diviner data.

405 Using the set of 154 topographically selected polar craters described in the Appendix, one
406 can look at the diameter-to-depth ratios of the fresh and anomalous craters relative to a set that
407 have been found without reference to their CPR properties. The mean diameter-to-depth ratios of
408 the fresh and anomalous craters are $D/d \sim 5.0$ and 5.9 respectively. Increasing D/d would be
409 expected as craters age, because the depths decrease over time while the diameters change little.
410 These measurements are therefore consistent with the picture of the anomalous craters being
411 older than the fresh ones. However, the topographically selected craters have even larger D/d
412 values, with a mean of ~ 7.0 . Could these differences be driven by the crater diameter-to-depth
413 ratio varying with crater size? Figure 15 shows the different crater sets as a function of crater
414 diameter. The solid black line represents the median D/d for the topographically selected craters
415 binned into three different diameter ranges, whereas the green line shows the relation found by
416 Pike (1974) for a set of fresh lunar craters. It is clear that the anomalous craters typically have
417 lower diameter-to-depth ratios than the set of polar craters selected only on topography. Under
418 the assumption that D/d is a proxy for crater age, one therefore infers that the anomalous craters,
419 while older than the fresh ones, are still less mature than typical craters in the north polar region.
420 This is again suggestive that the effects of micrometeorite bombardment on the steep crater walls
421 have not yet acted to remove all of the rocks or roughness that give rise to high CPR values.

422 If micrometeoritic bombardment is isotropic and the blocky debris from the crater forming
423 impacts is weathered away at similar rates inside and outside polar craters, then these results im-
424 ply that processes are preferentially acting on the steep slopes to refresh the near-surface rough-
425 ness to which the CPR is sensitive. This picture is consistent with the findings of Bandfield
426 et al. (2011), who use the thermal inertia determined from Diviner measurements to infer rock
427 abundances and regolith thicknesses. They find extra rockiness on steep crater walls relative to
428 crater floors and crater exteriors, which is in qualitative agreement with what is inferred in this

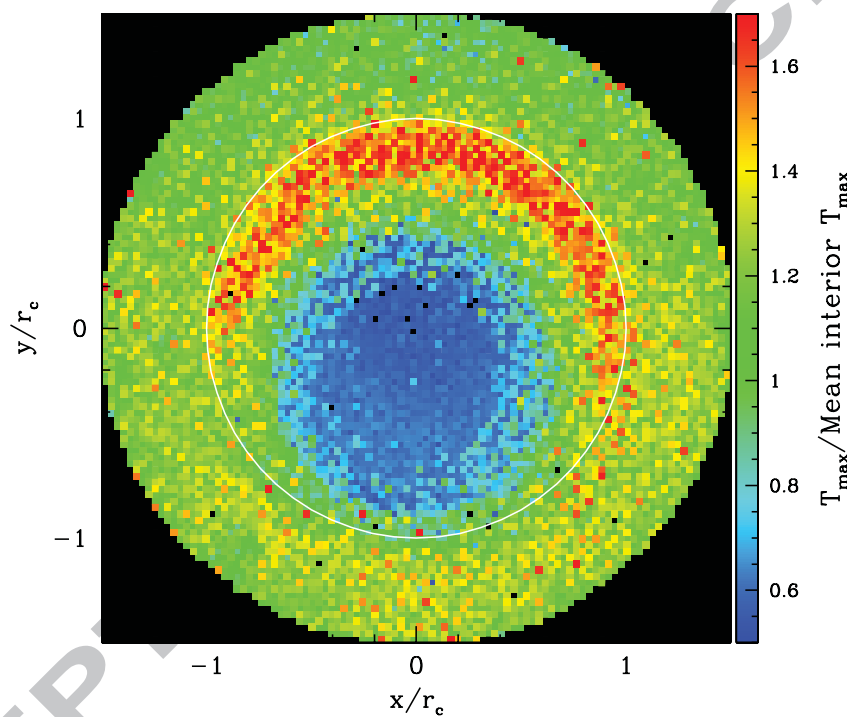


Figure 14: The stacked Diviner-inferred pixel T_{\max} relative to the mean within each crater for the 33 anomalous craters. North is upwards, so the relatively cold part of the average crater is pole-facing.

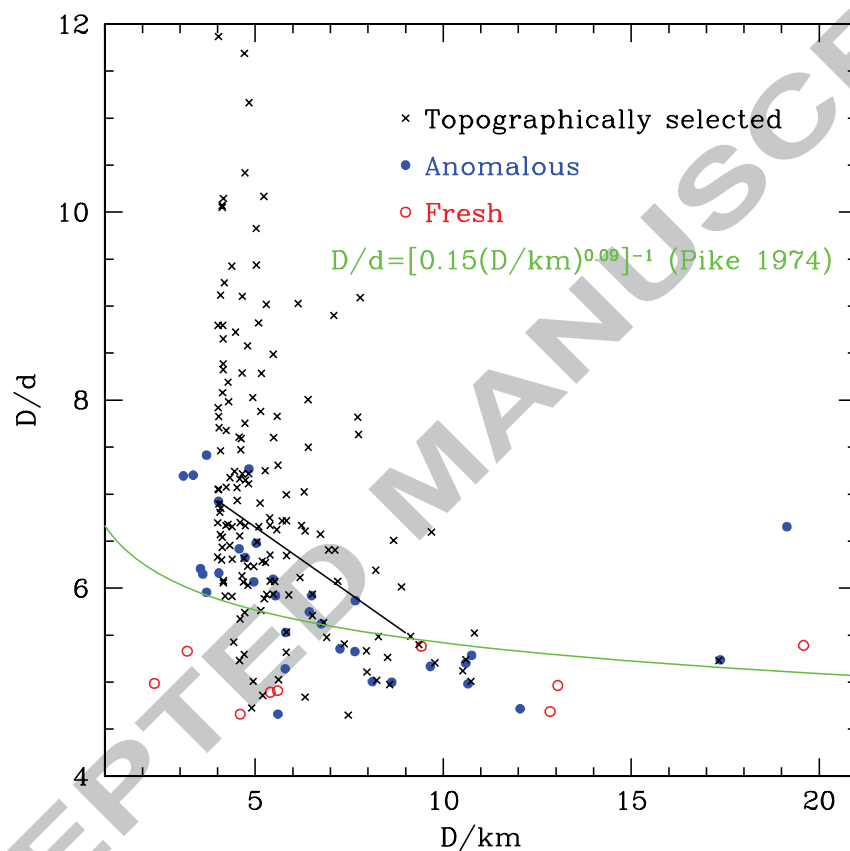


Figure 15: The variation of diameter-to-depth ratio (D/d) with crater diameter for the 33 anomalous craters (blue filled circles), 9 fresh craters (red open circles) and 154 topographically selected, isolated polar craters (black crosses). The black line represents the variation with diameter of the median of the black points, and the green line traces the relation given by Pike (1974) for fresh lunar craters.

study. Similarly, Fa and Cai (2013) use LROC images to show higher rock abundance interior to craters relative to their exteriors. Furthermore, they find this extra rockiness correlates with the difference between interior and exterior CPR values, as measured by Mini-RF. Both the Diviner and LROC rock abundances refer to objects that are at least 1 – 2 m in size, which is ~ 10 times the S-band radar wavelength. While there is no guarantee that rockiness on these relatively large scales implies roughness on scales more comparable with the radar wavelength, the modelling of Fa and Cai (2013) suggests that the larger rocks can nevertheless provide a significant CPR enhancement through dihedral reflections.

If the anomalous craters do have high CPR as a result of differential weathering of roughness, then the finding reported by Spudis et al. (2013), that the number density of anomalous craters at the poles greatly exceeds that at lower latitudes, remains to be explained. This apparent dependence on temperature is difficult to reconcile with the indifference to local temperature of the CPR distribution within anomalous polar craters. One would really like to start from the topographically-selected crater sample and study the variation of CPR with crater morphology, rather than starting from craters that have a particular CPR distribution, as was done here and in previous work. Looking only at CPR-selected craters can lead to a misleading impression of the population of craters as a whole. An orthorectified CPR mosaic, already tied to the LOLA DEM, would be necessary to avoid topographically-selected craters being ejected from the sample if their CPR was insufficiently distinct for them to be detected via their CPR, which has occurred in this study, as described in Section 2.4.

5. Conclusions

The distribution of pixel CPR values inside and outside fresh craters is largely independent of the angle of incidence with which the lunar surface is viewed. In contrast, for anomalous craters the angle of incidence has a large impact on the CPR maps that result. In these cases, counting pixels in SAR mosaics that have not been rectified for the effect of parallax has the effect of biasing the crater interior CPR pixel distribution to be dominated by observations of the near wall, viewed at larger incidence angle. Consequently, the mean interior crater CPR measured from an unrectified Mini-SAR map would exceed that for the crater exterior even when the interior and exterior surfaces have identical radar reflectivities (see Figure 9).

The typical variation of CPR with angle of incidence was measured within the anomalous craters and used to make a model to quantify how using unrectified mosaics will bias the distribution of pixel CPRs inside the crater relative to that from just outside. While this effect alone creates a sufficient change in the mean pixel CPR to explain some of the anomalous craters, the additional scatter required to recover the observed CPR distributions exceeds the statistical uncertainties on the measurements. Therefore, the CPR is also significantly affected by variations in the surface properties.

An additional variation with distance from the crater centre has also been discovered, with the crater centre having CPR values like those of the crater exterior, while larger CPR values at any given incidence angle are found on the steeper parts of the crater walls. It is argued that this variation of CPR with local slope, rather than local temperature, suggests that it results from a variation in the extent to which roughness is visible to the incident radar. Steeper walls near the angle of repose may be less able to sustain enough fine regolith to prevent the radar from seeing the rougher rocks underneath or it could just be that ongoing weathering produces more surface rocks or roughness on steeper slopes.

473 This argument is supported by the fact that anomalous craters, while having larger diameter-
474 to-depth ratios than fresh ones, are typically steeper-sided than craters determined using a crater-
475 finding algorithm applied to the LOLA DEM. Assuming that the diameter-to-depth represents
476 a proxy for crater age, the anomalous craters are of intermediate age. If surface roughness re-
477 freshed by mass-wasting on steep slopes were responsible for the high CPR, then one would
478 expect anomalous craters to be of intermediate age, because fresh craters have high CPR both
479 inside and outside, whereas old craters do not retain sufficiently steep sides for mass-wasting to
480 continue to promote sufficient surface roughness to cause high CPR. Thus, the surface roughness
481 explanation appears to pass this test.

482 Future analyses of the lunar SAR data should use properly controlled and rectified CPR
483 mosaics that are tied to the LOLA global DEM and take into account explicitly the dependence of
484 CPR on angle of incidence. The model of Fa et al. (2011), while not including multiple scattering
485 and the CBOE, suggests that radar data will not be able to distinguish between regolith with and
486 without a few wt% WEH, which is the level that the LCROSS and LPNS results imply is the
487 likely concentration. There is strong circumstantial evidence that the extractable information
488 from the lunar SAR data will pertain to surface or near-surface roughness rather than water ice.
489 This should provide fertile ground in conjunction with Diviner and LROC data sets to learn about
490 surface weathering as a function of local slope and composition (Bell et al., 2012).

491 Acknowledgments

492 VRE thanks Randy Kirk for helpful comments. We would like to thank the referees for their
493 helpful comments. This work was supported by the Science and Technology Facilities Council
494 [grant number ST/F001166/1]. LT acknowledges the support of the LASER and PGG NASA
495 programs for funding this research.

496 References

- 497 Bandfield, J. L., Ghent, R. R., Vasavada, A. R., Paige, D. A., Lawrence, S. J., Robinson, M. S., Dec. 2011. Lunar surface
498 rock abundance and regolith fines temperatures derived from LRO Diviner Radiometer data. *Journal of Geophysical*
499 *Research (Planets)* 116, E003866.
- 500 Bell, S. W., Thomson, B. J., Dyar, M. D., Neish, C. D., Cahill, J. T. S., Bussey, D. B. J., Nov. 2012. Dating small fresh
501 lunar craters with Mini-RF radar observations of ejecta blankets. *Journal of Geophysical Research (Planets)* 117,
502 E004007.
- 503 Butler, B. J., Aug. 1997. The migration of volatiles on the surfaces of Mercury and the Moon. *J. Geophys. Res.* 102,
504 19283–19292.
- 505 Campbell, B. A., Mar. 2002. Radar Remote Sensing of Planetary Surfaces.
- 506 Campbell, B. A., Jun. 2012. High circular polarization ratios in radar scattering from geologic targets. *Journal of Geo-*
507 *physical Research (Planets)* 117, 6008.
- 508 Campbell, D. B., Campbell, B. A., Carter, L. M., Margot, J.-L., Stacy, N. J. S., Oct. 2006. No evidence for thick deposits
509 of ice at the lunar south pole. *Nature* 443, 835–837.
- 510 Campbell, D. B., Chandler, J. F., Ostro, S. J., Pettengill, G. H., Shapiro, I. I., May 1978. Galilean satellites - 1976 radar
511 results. *Icarus* 34, 254–267.
- 512 Clark, R. N., Oct. 2009. Detection of Adsorbed Water and Hydroxyl on the Moon. *Science* 326, 562.
- 513 Colaprete, A., Schultz, P., Heldmann, J., Wooden, D., Shirley, M., Ennico, K., Hermalyn, B., Marshall, W., Ricco, A.,
514 Elphic, R. C., Goldstein, D., Summy, D., Bart, G. D., Asphaug, E., Korycansky, D., Landis, D., Sollitt, L., Oct. 2010.
515 Detection of Water in the LCROSS Ejecta Plume. *Science* 330, 463.
- 516 Crider, D. H., Vondrak, R. R., Nov. 2000. The solar wind as a possible source of lunar polar hydrogen deposits. *J.*
517 *Geophys. Res.* 105, 26773–26782.
- 518 Crider, D. H., Vondrak, R. R., Jun. 2003. Space weathering of ice layers in lunar cold traps. *Advances in Space Research*
519 31, 2293–2298.

- 520 Eke, V. R., Teodoro, L. F. A., Elphic, R. C., Mar. 2009. The spatial distribution of polar hydrogen deposits on the Moon.
521 Icarus 200, 12–18.
- 522 Fa, W., Cai, Y., Aug. 2013. Circular polarization ratio characteristics of impact craters from Mini-RF observations and
523 implications for ice detection at the polar regions of the Moon. Journal of Geophysical Research (Planets) 118, 1582–
524 1608.
- 525 Fa, W., Wieczorek, M. A., Heggy, E., Mar. 2011. Modeling polarimetric radar scattering from the lunar surface: Study
526 on the effect of physical properties of the regolith layer. Journal of Geophysical Research (Planets) 116, 3005.
- 527 Feldman, W. C., Maurice, S., Binder, A. B., Barraclough, B. L., Elphic, R. C., Lawrence, D. J., Sep. 1998. Fluxes of Fast
528 and Epithermal Neutrons from Lunar Prospector: Evidence for Water Ice at the Lunar Poles. Science 281, 1496–1500.
- 529 Freeman, T., 1991. Calculating catchment area with divergent flow based on a regular grid. Computers and Geosciences
530 17, 413–422.
- 531 Gladstone, G. R., Retherford, K. D., Egan, A. F., Kaufmann, D. E., Miles, P. F., Parker, J. W., Jan. 2012. Far-ultraviolet
532 reflectance properties of the Moon's permanently shadowed regions. Journal of Geophysical Research (Planets) 117,
533 E003913.
- 534 Hapke, B., Dec. 1990. Coherent backscatter and the radar characteristics of outer planet satellites. Icarus 88, 407–417.
- 535 Harmon, J. K., Slade, M. A., Vélez, R. A., Crespo, A., Dryer, M. J., Johnson, J. M., May 1994. Radar mapping of
536 Mercury's polar anomalies. Nature 369, 213–215.
- 537 Head, J. W., Fassett, C. I., Kadish, S. J., Smith, D. E., Zuber, M. T., Neumann, G. A., Mazarico, E., Sep. 2010. Global
538 Distribution of Large Lunar Craters: Implications for Resurfacing and Impactor Populations. Science 329, 1504.
- 539 Kirk, R. L., Becker, T. L., Shinaman, J., Edmundson, K. L., Cook, D., Bussey, D. B. J., Mar. 2013. A Radargrammetric
540 Control Network and Controlled Mini-RF Mosaics of the Moon's North Pole... at Last! In: Lunar and Planetary
541 Institute Science Conference Abstracts. Vol. 44 of Lunar and Planetary Institute Science Conference Abstracts. p.
542 2920.
- 543 Lawrence, D. J., Feldman, W. C., Elphic, R. C., Hagerty, J. J., Maurice, S., McKinney, G. W., Prettyman, T. H., Aug.
544 2006. Improved modeling of Lunar Prospector neutron spectrometer data: Implications for hydrogen deposits at the
545 lunar poles. Journal of Geophysical Research (Planets) 111, E08001.
- 546 Lawrence, D. J., Feldman, W. C., Goldsten, J. O., Maurice, S., Peplowski, P. N., Anderson, B. J., Bazell, D., McNutt,
547 R. L., Nittler, L. R., Prettyman, T. H., Rodgers, D. J., Solomon, S. C., Weider, S. Z., Jan. 2013. Evidence for Water
548 Ice Near Mercury's North Pole from MESSENGER Neutron Spectrometer Measurements. Science 339, 292.
- 549 Nozette, S., Lichtenberg, C. L., Spudis, P., Bonner, R., Ort, W., Malaret, E., Robinson, M., Shoemaker, E. M., Nov. 1996.
550 The Clementine Bistatic Radar Experiment. Science 274, 1495–1498.
- 551 Nozette, S., Spudis, P., Bussey, B., Jensen, R., Raney, K., Winters, H., Lichtenberg, C. L., Marinelli, W., Crusan,
552 J., Gates, M., Robinson, M., Jan. 2010. The Lunar Reconnaissance Orbiter Miniature Radio Frequency (Mini-RF)
553 Technology Demonstration. Space Sci. Rev. 150, 285–302.
- 554 O'Callaghan, J. F., Mark, D. M., 1984. The extraction of drainage networks from digital elevation data. Computer Vision,
555 Graphics, and Image Processing 28, 323–344.
- 556 Ostro, S. J., Campbell, D. B., Simpson, R. A., Hudson, R. S., Chandler, J. F., Rosema, K. D., Shapiro, I. I., Standish,
557 E. M., Winkler, R., Yeomans, D. K., Nov. 1992. Europa, Ganymede, and Callisto - New radar results from Arecibo
558 and Goldstone. J. Geophys. Res. 97, 18227.
- 559 Paige, D. A., Siegler, M. A., Zhang, J. A., Hayne, P. O., Foote, E. J., Bennett, K. A., Vasavada, A. R., Oct. 2010. Diviner
560 Lunar Radiometer Observations of Cold Traps in the Moon's South Polar Region. Science 330, 479.
- 561 Pieters, C. M., Goswami, J. N., Clark, R. N., Annadurai, M., Boardman, J., Buratti, B., Combe, J.-P., Oct. 2009. Character
562 and Spatial Distribution of OH/H₂O on the Surface of the Moon Seen by M³ on Chandrayaan-1. Science 326, 568.
- 563 Pike, R. J., Nov. 1974. Depth/diameter relations of fresh lunar craters - Revision from spacecraft data. Geophys. Res.
564 Lett. 1, 291–294.
- 565 Raney, R. K., Nov. 2007. Hybrid-Polarity SAR Architecture. IEEE Transactions on Geoscience and Remote Sensing 45,
566 3397–3404.
- 567 Salamunićar, G., Lončarić, S., Mazarico, E., Jan. 2012. LU60645GT and MA132843GT catalogues of Lunar and
568 Martian impact craters developed using a Crater Shape-based interpolation crater detection algorithm for topography
569 data. P&SS 60, 236–247.
- 570 Simpson, R. A., Tyler, G. L., Feb. 1999. Reanalysis of Clementine bistatic radar data from the lunar South Pole. J.
571 Geophys. Res. 104, 3845–3862.
- 572 Smith, D. E., Zuber, M. T., Neumann, G. A., Lemoine, F. G., Mao, D.-d., Smith, J. C., Bartels, A. E., Sep. 2010. Initial
573 observations from the Lunar Orbiter Laser Altimeter (LOLA). Geophys. Res. Lett. 37, 18204.
- 574 Spudis, P. D., Bussey, D. B. J., Baloga, S. M., Butler, B. J., Carl, D., Carter, L. M., Chakraborty, M., Mar. 2010. Initial
575 results for the north pole of the Moon from Mini-SAR, Chandrayaan-1 mission. Geophys. Res. Lett. 37, 6204.
- 576 Spudis, P. D., Bussey, D. B. J., Baloga, S. M., Cahill, J. T. S., Glaze, L. S., Patterson, G. W., Raney, R. K., Thompson,
577 T. W., Thomson, B. J., Ustinov, E. A., Oct. 2013. Evidence for water ice on the moon: Results for anomalous polar
578 craters from the LRO Mini-RF imaging radar. Journal of Geophysical Research (Planets) 118, 2016–2029.

- 579 Spudis, P. D., Bussey, D. B. J., Butler, B., Carter, L., Gillis-Davis, J., Goswami, J., Heggy, E., Kirk, R., Misra, T.,
580 Nozette, S., Robinson, M. S., Raney, R. K., Thomson, B., Ustinov, E., Mar. 2009. The Mini-SAR Imaging Radar on
581 the Chandrayaan-1 Mission to the Moon. In: Lunar and Planetary Institute Science Conference Abstracts. Vol. 40 of
582 Lunar and Planetary Institute Science Conference Abstracts. p. 1098.
- 583 Stacy, N. J. S., Campbell, D. B., Ford, P. G., 1997. Arecibo radar mapping of the lunar poles: A search for ice deposits.
584 Science 276, 1527–1530.
- 585 Sunshine, J. M., Farnham, T. L., Feaga, L. M., Groussin, O., Merlin, F., Milliken, R. E., A'Hearn, M. F., Oct. 2009.
586 Temporal and Spatial Variability of Lunar Hydration As Observed by the Deep Impact Spacecraft. Science 326, 565.
- 587 Teodoro, L. F. A., Eke, V. R., Elphic, R. C., Jun. 2010. Spatial distribution of lunar polar hydrogen deposits after
588 KAGUYA (SELENE). Geophys. Res. Lett. 37, 12201.
- 589 Thompson, T. W., Ustinov, E. A., Heggy, E., Jan. 2011. Modeling radar scattering from icy lunar regoliths at 13 cm and
590 4 cm wavelengths. Journal of Geophysical Research (Planets) 116, 1006.
- 591 Thomson, B. J., Bussey, D. B. J., Neish, C. D., Cahill, J. T. S., Heggy, E., Kirk, R. L., Patterson, G. W., Raney, R. K.,
592 Spudis, P. D., Thompson, T. W., Ustinov, E. A., Jul. 2012. An upper limit for ice in Shackleton crater as revealed by
593 LRO Mini-RF orbital radar. Geophys. Res. Lett. 39, 14201.
- 594 Vasavada, A. R., Paige, D. A., Wood, S. E., Oct. 1999. Near-Surface Temperatures on Mercury and the Moon and the
595 Stability of Polar Ice Deposits. Icarus 141, 179–193.
- 596 Watson, K., Murray, B., Brown, H., May 1961. On the Possible Presence of Ice on the Moon. J. Geophys. Res. 66,
597 1598–1600.

598 Appendix A. Crater-finding algorithm

599 The list of craters produced by Head et al. (2010) from the LOLA topographical data consists
600 of 5185 craters with radii of at least 10 km distributed over the entire lunar surface. Salamunićar
601 et al. (2012) supplemented this with additional craters found using a predominantly automated
602 detection algorithm that was based on the LOLA DEM. Their crater catalogue contained 60645
603 objects and is the most complete to radii of 4 km. For the purpose of this study, even smaller
604 craters in the vicinity of the lunar north pole are of interest, and the desire is to produce craters
605 with representative diameter-to-depth ratios. Thus, an algorithm has been developed to find
606 simple craters with radii in the range $2 \leq r_c/\text{km} \leq 10$ using the LOLA north polar stereographic
607 digital elevation map.

608 The crater-finding algorithm consists of two main stages. First, by placing ‘water’ on the
609 surface and letting it drain downhill to create puddles, a set of potential crater centres are found.
610 The amount of water in each puddle reflects the area from which it came and hence provides an
611 estimate of the radius of the potential crater. Secondly, in the vicinity of each potential crater, the
612 Laplacian of the topography is filtered to search for circularly symmetric patterns with a concave
613 centre surrounded by a convex rim. The details of these two parts of the algorithm are described
614 in the following subsections.

615 Appendix A.1. Finding crater candidates

616 Candidates for crater centres are found using a hydrological algorithm that is a simplified
617 version of those described by O’Callaghan and Mark (1984) and Freeman (1991). A smoothed
618 version of the LOLA polar stereographic 80 m DEM is used. The smoothing suppresses small
619 scale depressions that might otherwise prevent ‘water’ from draining further into larger depres-
620 sions. It also removes candidate tiny craters that might be within other craters, which would
621 consequently fail the isolation criterion described in the next section and be jettisoned from the
622 sample. A single smoothing entails replacing each altitude with a value that is $1/4$ of the original
623 value plus $1/8$ of each of the values in the 4 adjacent pixels, plus $1/16$ times the values in the
624 diagonally adjacent pixels. Given that craters in the radius range 2 – 10 km are being considered
625 here, 3 smoothings of the DEM are used.

An amount of ‘water’ proportional to the pixel area is placed into each pixel in the smoothed digital elevation map and this is allowed to run downhill using the following iterative method. Each pixel with none of its 8 neighbours being higher and containing water, distributes its water to neighbouring pixels that are lower than it. The water is distributed to the N lower neighbouring pixels in proportion to the gradient in their direction. Thus, the fraction of water sent to the i th lower neighbour is given by

$$f_i = \frac{|\nabla_i|}{\sum_{j=1}^N |\nabla_j|}, \quad (\text{A.1})$$

where ∇_i represents the gradient in the direction of the i th neighbour. This draining is repeated until no pixels with lower neighbours contain any water, at which point the set of ‘wet’ pixels defines the centres of crater candidates, with the amount of water providing an estimate of the potential crater radius under the assumption that it came from a circular patch of the surface.

Appendix A.2. Confirming craters

For the purpose of this study, there is no need to have a complete sample of craters, merely one that is representative of the diameter-to-depth ratios of craters as a whole. Thus, for simplicity, only isolated crater candidates are retained for further consideration. Isolation is defined as having no other crater candidate within one candidate crater radius from the candidate crater centre. This yields a set of ~ 68000 candidate isolated craters of all radii at latitude $> 80^\circ$. These candidates are then filtered to refine the centres and radii and determine a statistic related to how much they match a simple crater in their topographic profile.

The Laplacian of the DEM in the vicinity of each of these potential craters is filtered using a compensated filter of the form

$$w(r) = \begin{cases} N_{\text{ring}}/N_{\text{cen}} & \text{if } r < 0.6r_{\text{c,test}}, \\ -1 & \text{if } |r - r_{\text{c,test}}| \leq 40\text{m}, \\ 0 & \text{otherwise,} \end{cases} \quad (\text{A.2})$$

where $r_{\text{c,test}}$ is the crater radius being tested, N_{cen} is the number of 80 m pixel centres lying within a disc of radius $0.6r_{\text{c,test}}$ and N_{ring} is the number of pixel centres within an annulus one pixel wide having mean radius equal to $r_{\text{c,test}}$. Crater radii are tested in the range $0.5 - 1.5$ times the value inferred from the amount of water gathered by each candidate. This filter picks out regions that have a concave disc of surface surrounded by a convex rim-like structure. The pixels within which the maximum filtered Laplacian values are found for each tested crater radius provide the most likely crater centres for those test radii.

To determine which tested radius produces the best overall match, a significance of the value of the filtered Laplacian is defined. Applying the filter to a random part of the Laplacian map inferred from the DEM would give rise to a distribution of filter values. This can be treated as a random walk with a step size of the rms Laplacian weighted by the rms step size of the filter. Using this to normalise the filtered Laplacian values around the candidate crater centre gives a significance for each candidate crater. This value is used to determine the best test radius. Each candidate with a significance, S , (of the filtered Laplacian relative to that expected from a random walk) of at least $S_{\text{min}} = 15$ is deemed to be a detected crater.

Appendix A.3. The set of polar craters

The algorithm described above yields 154 craters with latitude greater than 80° . Table A1 contains a list of the centres and radii of these north polar, isolated craters, and Figure A.16

664 shows their distribution with diameter. Figure 15 plots the dependence of the crater diameter-
 665 to-depth ratios on diameter, illustrating how these topographically selected craters typically have
 666 shallower profiles than either the fresh or anomalous craters studied by Spudis et al. (2010).

667 The choice of S_{\min} feeds into the inferred diameter-to-depth ratio of the resulting crater cata-
 668 logue, because deeper craters better match the filter shape than shallower ones. Thus, increasing
 669 S_{\min} from 15 to 20 decreases the number of craters from 154 to 108, and the diameter-to-depth
 670 ratio from 7.0 to 6.3. However, the lower threshold of $S_{\min} = 15$ still produces a set of az-
 671 imuthally symmetric depressions with convex rims that are crater-like. Figure A.17 shows the
 672 azimuthally-averaged height profiles, scaled by crater radius, of all 154 craters with $S > 15$. The
 673 diversity of depths reflects the range of diameter-to-depth values for the selected craters, and it is
 674 apparent that each of the craters possesses both a central depression and a convex rim.

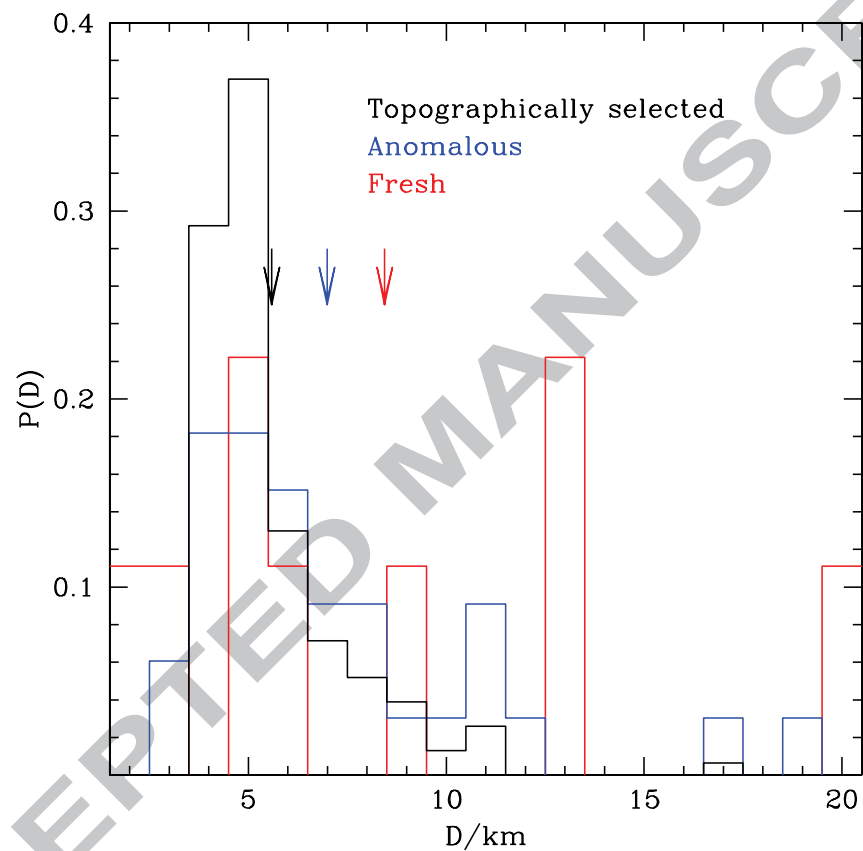


Figure A.16: The probability distributions of the crater diameters for the three different sets of craters: 154 topographically selected (black), 9 fresh (red) and 33 anomalous (blue). Coloured arrows show the mean diameters in each sample.

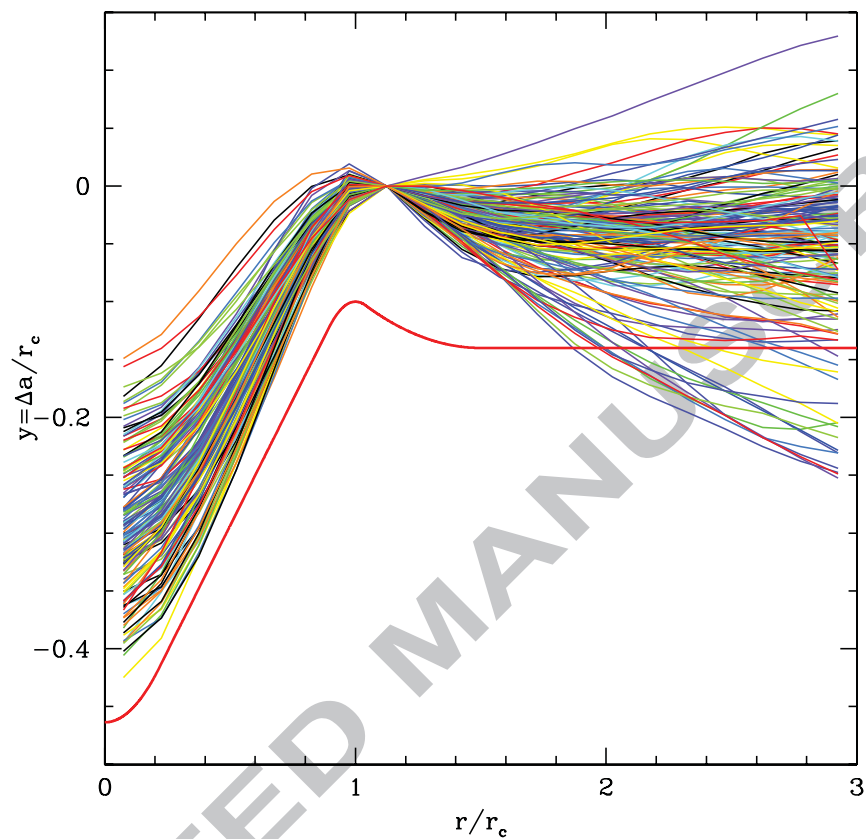


Figure A.17: The azimuthally averaged height profiles, scaled by crater radius, for the 154 topographically selected craters. Each radius is rescaled by the crater radius, r_c , whereas the scaled height is plotted relative to the value at $r/r_c = 1.1$. The bold red line shows the profile for the model crater used in Section 3.2, offset vertically by 0.1 for clarity.

Table A.2: Radii and locations for the 154 topographically selected isolated craters. Longitudes and latitudes are given in degrees.

Crater #	r_c /km	(lat,lon)	Crater #	r_c /km	(lat,lon)	Crater #	r_c /km	(lat,lon)	Crater #	r_c /km	(lat,lon)
1	2.4	80.01, -21.4	2	2.7	80.01, 31.8	3	2.1	81.12, -21.4	4	2.9	81.35, 19.0
5	4.9	81.65, -23.9	6	2.6	82.26, 11.7	7	2.4	81.84, 28.2	8	2.3	81.49, -32.9
9	2.7	81.85, 29.2	10	2.1	81.83, -31.1	11	2.1	80.07, -46.6	12	2.2	81.98, -34.3
13	3.9	82.65, 26.7	14	2.0	83.29, -13.7	15	2.7	82.07, -37.1	16	2.5	83.06, 24.5
17	8.7	80.26, -50.1	18	2.0	82.49, -34.2	19	2.8	83.87, -7.4	20	5.3	83.76, -13.9
21	2.5	82.68, -37.4	22	2.4	84.12, 15.7	23	3.6	80.80, 53.7	24	2.0	84.14, -21.7
25	2.2	84.18, -20.4	26	2.3	84.64, -6.2	27	2.3	80.01, 61.6	28	2.0	81.87, -56.8
29	2.1	81.43, 59.7	30	4.3	80.16, -66.1	31	3.7	80.32, 65.9	32	3.7	85.78, 25.2
33	2.9	85.91, -27.7	34	2.1	83.64, -55.7	35	3.5	80.46, -68.7	36	2.8	81.19, -68.2
37	4.8	83.89, -57.4	38	2.3	84.88, -50.7	39	2.6	83.94, -59.3	40	2.8	85.75, 43.6
41	2.2	81.40, 69.7	42	2.1	84.57, -56.7	43	2.4	85.30, -52.3	44	2.3	81.08, 71.8
45	5.4	86.99, 28.6	46	2.3	85.79, 54.0	47	3.5	81.85, 72.8	48	3.2	87.12, -33.4
49	2.0	86.89, -45.6	50	2.0	87.52, -29.3	51	2.5	87.69, 30.8	52	2.6	83.91, 72.4
53	2.1	84.51, -70.6	54	2.7	81.47, -77.8	55	2.4	82.80, 75.5	56	2.9	87.97, 29.9
57	2.7	86.64, 58.5	58	2.3	88.08, -27.8	59	2.6	84.90, -71.5	60	2.1	88.22, -26.0
61	3.4	88.26, 25.2	62	3.4	81.50, -79.8	63	2.7	88.08, 39.9	64	3.1	87.92, 57.1
65	3.1	87.66, 63.2	66	2.4	85.59, 76.9	67	4.7	87.36, 68.0	68	2.2	86.01, 76.0
69	2.5	86.65, 73.7	70	3.2	85.75, 78.1	71	2.1	87.81, -66.8	72	2.5	88.75, 47.0
73	2.3	82.66, -83.6	74	3.2	81.56, -84.6	75	3.3	88.19, 63.4	76	2.6	85.56, 79.5
77	2.6	88.96, -45.1	78	3.9	88.05, 68.4	79	2.8	82.71, -87.1	80	2.9	81.22, 88.4
81	2.4	83.32, 88.2	82	4.1	87.13, -86.3	83	2.6	85.97, 88.1	84	2.0	89.64, -108.8
85	2.6	86.27, 94.0	86	2.0	86.89, 96.4	87	2.3	83.65, 93.7	88	2.0	88.17, 112.0
89	2.0	87.69, 107.9	90	2.4	87.83, 113.0	91	2.5	85.43, 101.1	92	3.4	87.41, 110.0
93	2.7	80.43, -99.5	94	2.0	88.41, -177.9	95	2.1	84.87, -109.0	96	2.1	81.87, -102.2
97	2.1	82.54, 105.1	98	2.4	83.09, -106.4	99	2.1	87.24, 135.7	100	2.5	83.74, -108.7
101	3.6	83.35, -108.3	102	2.5	84.00, -110.7	103	2.1	81.40, -104.7	104	2.9	84.55, -114.5
105	3.9	82.41, 107.5	106	2.0	87.66, 172.3	107	2.5	84.72, -116.9	108	2.2	81.45, 106.2
109	2.4	85.94, -129.2	110	3.1	80.51, 107.7	111	2.1	81.85, 110.8	112	2.4	86.64, 152.8
113	2.2	85.63, -134.4	114	2.4	84.62, 125.5	115	5.4	82.63, 116.0	116	2.0	85.15, 132.9
117	2.3	85.24, 136.3	118	2.4	81.54, -114.6	119	2.6	81.01, 113.5	120	2.0	84.44, -130.7
121	2.4	84.00, -127.4	122	3.2	84.49, -132.4	123	2.2	86.18, -177.6	124	2.2	85.85, -157.1
125	4.4	81.08, 115.8	126	2.0	83.37, 126.1	127	4.1	80.93, -115.6	128	2.2	81.45, 118.2
129	4.0	83.10, 129.9	130	3.2	83.73, -135.3	131	4.0	80.45, -122.7	132	4.1	82.24, -134.2
133	4.3	84.05, -156.4	134	3.3	80.17, -124.6	135	2.3	80.58, 126.4	136	2.6	84.10, -163.4
137	2.1	83.22, 147.8	138	2.9	83.99, 174.0	139	2.1	84.00, -176.2	140	2.3	82.90, 150.9
141	4.6	82.46, 145.7	142	5.3	81.15, 137.7	143	2.3	80.31, -135.4	144	2.3	80.74, 146.0
145	2.3	80.97, -161.1	146	2.1	81.29, 171.3	147	2.1	80.97, -162.7	148	4.3	80.46, -155.1
149	2.7	80.38, -156.1	150	2.6	80.71, 164.1	151	2.1	80.96, 172.6	152	2.9	80.27, 158.6
153	2.8	80.84, 173.3	154	2.1	80.18, 176.4						

Highlights:

- We consider the variation of CPR with position within anomalous polar craters.
- The increase of CPR with incidence angle is quantified.
- CPR in the centres of anomalous craters is indistinguishable from that outside.
- High CPR is located on crater walls and does not correlate with temperature.
- We introduce a crater-finding algorithm and show anomalous craters are of intermediate age.